Optimal Array-Pattern Synthesis for Wideband Digital Transmit Arrays

Dan P. Scholnik, *Member, IEEE*, and Jeffrey O. Coleman, *Senior Member, IEEE*

***Abstract*—Some next-generation radio frequency systems are expected to share a common transmit aperture among multiple users across a wide range of frequencies and functions such as radar and communications. The requisite linear architectures and digital signal generation will permit far greater flexibility in the design of array patterns than traditional time-delay steered wideband transmit arrays. Merely replicating the traditional architecture in digital signal processing would generally represent an inefficient use of computational resources; thus, we propose instead to place a finite-impulse response filter per input signal at each element and to directly optimize the resulting wideband array pattern. For this architecture, we present a passband-equivalent transmit-array model and derive expressions for wideband directivity, efficiency, error sensitivity, gain, peak and mean-square sidelobes, mainlobe frequency-response flatness, and polarization. All can be constrained using second-order cone programming, a highly-efficient type of convex optimization. Several examples illustrate the design tradeoffs, including the need to limit undesirable superdirective effects in wideband arrays. The system model and the derivations are general enough to admit almost any array architecture, including arbitrary element locations, nonuniform element responses, and multiple polarizations.**

***Index Terms*—Antenna arrays, array signal processing, optimization methods, second-order cone programming.**

I. Introduction

WIDEBAND antenna arrays in which the array patterns are primarily determined by digital processing have been enabled by the continued evolution of data converters and digital signal processing (DSP) capability. Formerly, wideband arrays required switched analog delay elements and attenuators, but now the array patterns can be controlled by digital filtering the data for each antenna element, with the usual DSP gains in precision and flexibility. A conventional approach to digital pattern synthesis is to simply approximate the analog hardware with digital filters, but this has the same drawback as the analog system it replaces: artificial restrictions on the resulting array pattern. In most cases even ideal time-delay steering results in a suboptimal array response. It seems appropriate to rethink the problem of optimal wideband array pattern design from first principles, since the tools now exist [1]–[4] to solve large convex programs.

Manuscript received February 6, 2007; revised September 4, 2007. This work was supported by the Office of Naval Research and by the Naval Research Laboratory base program. The associate editor coordinating the review of this paper and approving it for publication was Dr. Alex Gershman.

The authors are with the Naval Research Laboratory, Radar Division, Code 5328, Washington, DC 20375 USA (e-mail: dan.scholnik@nrl.navy.mil; jeffrey.coleman@nrl.navy.mil).

Color versions of one or more of the figures in this paper are available online at http://ieeexplore.ieee.org.

Digital Object Identifier 10.1109/JSTSP.2007.909371

A. Background

Narrowband array-pattern design is a well-studied topic. The earliest works were analytical, predating widespread use of numerical optimization. Examples include Dolph's use of Chebychev polynomials to create equiripple array patterns [5] and Taylor's classic line-source distribution [6], which in its sampled form is widely used in arrays. It has long been recognized that there is a direct relationship between the array pattern of a uniform narrowband array and the frequency response of a multidimensional FIR filter [7]. This idea was extended to wideband array patterns in the form of fan [8] and cone [9] filters, where the names indicate the passband/stopband shape of a 2-D (fan) or 3-D (cone) filter that will pass/suppress plane waves from a given set of directions over a range of frequencies. (The underlying geometry of plane-wave spectra will be considered in Section II-C5.)

Since array patterns are in essence multidimensional finite-impulse response (FIR) filters, many of the same optimization tools that are used to design 1-D FIR filters can be used to design array patterns. Like FIR-filter frequency responses, array patterns are linear in the underlying beamformer coefficients; since most of the constraints of interest are either linear or convex quadratic functions of the coefficients, the resulting optimization problems are convex. Convex optimization techniques used for array-pattern design include second-order cone programming [10]–[14], semidefinite programming [15], and iterative least-squares [16]–[18]. Not all potential constraints are convex, notably unit-magnitude constraints needed to obtain a phase-only solution. Further, sometimes it is desired to optimize the element positions. Such problems can have many local minima and be difficult to solve. Approaches include iterative least-square methods to find local minima [17] or nongradient global methods such as genetic algorithms and simulated annealing [19]; none guarantee a global solution. We shall limit ourselves to convex optimization, which is sufficient for most designs.

Previous array-pattern synthesis papers that considered wideband design generally used one of three approaches. The first is to perform multiple independent narrowband designs over a range of frequencies [17]. The second is to optimize the narrowband weights of a delay-and-sum beamformer [19], which results in an array pattern that scales with temporal frequency. The third, *frequency-invariant* synthesis [14], [20], uses independent filters at each element to design an array pattern that is the same (to within acceptable error) at all frequencies in a band of interest. By contrast, we continue our earlier approach [11]–[13], [21] of simultaneously optimizing FIR filter coefficients for all elements subject to a set of wideband constraints based on actual system metrics. Depending on the constraints used, the results range from a delay-and-sum beamformer with

1932-4553/$25.00 © 2007 IEEE

jointly optimized delay filters to an array pattern that is approximately frequency invariant over most of the mainlobe. Examples of both are shown in the sequel.

This paper focuses on transmit arrays, although reciprocity could be invoked to apply many of the results to receive arrays. Transmit arrays have been considered for optimization far less frequently than receive arrays due to stricter hardware requirements on transmit in classical architectures. Chief among these is the use of saturated amplifiers for reasons of power efficiency. In contrast, we here anticipate the emergence of digital arrays that use some form of linear amplification to allow undistorted transmission of multiple simultaneous signals. This might take the form of discrete linear amplifiers or recently-proposed linear power-DAC architectures using temporal and spatio-temporal [22], [23] delta-sigma modulation.

B. Differences From Conventional Narrowband Design

We highlight here some significant differences between this work and conventional narrowband array theory. Having assumed a linear transmit array, we include in our system model multiple simultaneous input signals and corresponding independent array patterns for each input. Whereas narrowband signals are by definition approximated by sinusoids, wideband signals may exhibit significant spectral features. A consequence of the richer signal content is that standard narrowband array metrics such as directivity and gain become signal-dependent in the wideband case. When actual signal spectra are unknown or too numerous, we can choose a representative reference spectrum, such as that of bandlimited noise. In addition, the input signals may be deterministic or random. For simplicity, only the deterministic-signal analysis is presented here; in [22] both deterministic and random-signal analysis is presented in parallel. In most cases both approaches lead to identical array-pattern optimizations.

C. Structure of the Paper

The remainder of this paper is effectively divided into two parts. In Section II a general passband-equivalent model of a wideband digital transmit array is introduced and analyzed from the input through far-field radiation. The key result is the derivation of the wideband array pattern. The second part of the paper, comprising Sections III and IV, formulates various performance metrics for wideband arrays in terms of the wideband array pattern. As the metrics are derived, they are used to optimize an example array in a running series of example designs. This allows direct comparison of the various design approaches and demonstrates the importance of proper optimization criteria for wideband array patterns.

II. Analysis of the Wideband Array Model

We begin this section with a brief introduction to the notation and measure representation of signals and systems that will be used throughout, followed by a description of the passband-equivalent wideband transmit-array model. Signals are then traced from the input to the array element currents, with key system components described along the way.

A. Signals and Systems Representation

1) Notation: Scalar variables and scalar-valued functions are represented using medium-weight fonts: a, A. Vectors, matrices, and vector- or matrix-valued functions are indicated using a bold font: $\boldsymbol{a}, \boldsymbol{A}$. Measures in both functional and differential forms are indicated with an underbar: $\underline{a}, d\underline{a}$, except for the special case of Lebesgue measure dt. Common vector/matrix operations include transpose $\boldsymbol{A}^T$, conjugate $\boldsymbol{A}^*$, and conjugate transpose $\boldsymbol{A}^H$. The element in the mth row and the nth column of matrix $\boldsymbol{A}$ can be indicated either explicitly as $[\boldsymbol{A}]_{m,n}$ or implicitly as $A_{m,n}$, while the mth element of a vector $\boldsymbol{b}$ is indicated similarly as $[\boldsymbol{b}]_m$ or b_m. The nth column of matrix $\boldsymbol{A}$ is indicated by $[\boldsymbol{A}]_n$ or $\boldsymbol{A}_n$. The length $||\boldsymbol{x}|| = \sqrt{\boldsymbol{x}^H\boldsymbol{x}}$ of a vector $\boldsymbol{x}$ is the standard Euclidean norm, while the unit-vector operator $\hat{\boldsymbol{x}} \triangleq \boldsymbol{x}/||\boldsymbol{x}||$ is indicated with a hat. For electromagnetic field quantities such as the electric field $\vec{\boldsymbol{\varepsilon}}$, the 3-D vector nature is emphasized using an overarrow. Finally, sets $\boldsymbol{\mathcal{X}}, \mathcal{T}$ are indicated using a calligraphic font and use a bold font if the elements of the set are vectors or matrices.

2) Measure-Signal Representation: The signals at various points in a wideband array model may be discrete or continuous in either space or time. Rather than tediously define each operation (convolution, Fourier transform) for each combination, we represent signals with complex measures as in [24] and in the spirit of [25], [26] (which use generalized functions rather than measures). For example, the delayed point measure ${}_\tau\underline{\delta}(\mathcal{T}) \triangleq 1_{\mathcal{T}}(\tau)$, where $1_{\mathcal{T}}$ is the indicator function on set $\mathcal{T}$, formalizes the common engineering use of the shifted Dirac delta "function" $\delta(t-\tau)$ while counting measure $\underline{\sum}_{\boldsymbol{\mathcal{L}}}$ on a set $\boldsymbol{\mathcal{L}}$ formalizes arbitrary collections of impulses and impulse trains. In this framework a discrete-space, continuous-time signal (for example) can be variously represented as

$$\underline{a}(\boldsymbol{\mathcal{X}} \times \mathcal{T}) = \int_{\boldsymbol{\mathcal{X}}\times\mathcal{T}} \underline{a}(d\boldsymbol{x}, dt) = \int_{\boldsymbol{\mathcal{X}}} \underline{a}(d\boldsymbol{x}, \mathcal{T}) = \int_{\mathcal{T}} \underline{a}(\boldsymbol{\mathcal{X}}, dt)$$
$$= \int_{\mathcal{T}} \int_{\boldsymbol{\mathcal{X}}} a(\boldsymbol{x}, t) d\underline{\sum}_{\boldsymbol{\mathcal{L}}}(\boldsymbol{x}) dt.$$

The first line, not specific to the signal support, shows the equivalence on the measurable rectangles between the functional (left) and fully and partially differential forms of the measure; we will favor the fully differential form as it more closely resembles classical engineering notation. We write the differential form as $\underline{a}(d\boldsymbol{x}, dt)$ rather than the more conventional $d\underline{a}(\boldsymbol{x}, t)$ so that the arguments may be used to disambiguate differential measures on space-time from, for example, a spatial measure $\underline{a}(d\boldsymbol{x}, t)$ that is parametrized on time. The second line relates the measure representation to the usual functional form, where ordinary function a is the *density*, or *Radon-Nikodym* derivative [27], of the measure signal $\underline{a}$ with respect to *reference measure* $d\underline{\sum}_{\boldsymbol{\mathcal{L}}}(\boldsymbol{x})dt$, the product measure of $\boldsymbol{\mathcal{L}}$-counting measure on space and Lebesgue measure on time. We assume that Fubini's theorem is satisfied and show nested integrals. This decomposition cleanly separates the support of a signal (given by the reference measure) from its value (given by the density).

3) Fourier and Linear System Representations: With the measure representation, standard system operations can be

defined independent of signal class. The Fourier–Stieltjes transform [28] can be applied to a measure signal on time, space, or both

$$\underline{\boldsymbol{A}}(\boldsymbol{\mathcal{X}}, f) \triangleq \int e^{-\mathrm{j}2\pi f t}\underline{\boldsymbol{a}}(\boldsymbol{\mathcal{X}}, dt)$$
$$\underline{\mathbf{a}}(\boldsymbol{v}, \mathcal{T}) \triangleq \int e^{-\mathrm{j}2\pi \boldsymbol{v}\cdot\boldsymbol{x}}\underline{\boldsymbol{a}}(d\boldsymbol{x}, \mathcal{T})$$
$$\mathbf{A}(\boldsymbol{v}, f) \triangleq \int e^{-\mathrm{j}2\pi(\boldsymbol{v}\cdot\boldsymbol{x}+ft)}\underline{\boldsymbol{a}}(d\boldsymbol{x}, dt).$$

The first two are still measures on space and time, respectively. We use upper-case and upright fonts to indicate temporal and spatial Fourier transform, respectively. Linear space-invariant (LSI) and/or time-invariant (LTI) filters are also represented as complex measures with the filter output defined as a measure convolution [28] in time, space, or both

$$(\underline{\boldsymbol{h}} * \underline{\boldsymbol{a}})(\boldsymbol{\mathcal{X}} \times \mathcal{T}) \triangleq \int \underline{\boldsymbol{h}}(\mathcal{T} - \boldsymbol{\tau})\underline{\boldsymbol{a}}(\boldsymbol{\mathcal{X}}, d\boldsymbol{\tau})$$
$$(\underline{\boldsymbol{h}} \bigcirc \underline{\boldsymbol{a}})(\boldsymbol{\mathcal{X}} \times \mathcal{T}) \triangleq \int \underline{\boldsymbol{h}}(\boldsymbol{\mathcal{X}} - \boldsymbol{x})\underline{\boldsymbol{a}}(d\boldsymbol{x}, \mathcal{T})$$
$$(\underline{\boldsymbol{h}} \circledast \underline{\boldsymbol{a}})(\boldsymbol{\mathcal{X}} \times \mathcal{T}) \triangleq \int \underline{\boldsymbol{h}}\left(\boldsymbol{\mathcal{X}} \times \mathcal{T} - (\boldsymbol{x}, \boldsymbol{\tau})\right)\underline{\boldsymbol{a}}(d\boldsymbol{x}, d\boldsymbol{\tau}).$$

Spatial filtering may also be space-varying (LSV); here the filter is represented by a space-time measure with an extra spatial parameter and the output is defined as

$$(\underline{\boldsymbol{h}} \boxtimes \underline{\boldsymbol{a}})(\boldsymbol{\mathcal{X}} \times \mathcal{T}) \triangleq \int \underline{\boldsymbol{h}}\left(\boldsymbol{\mathcal{X}} \times (\mathcal{T} - \boldsymbol{\tau}); -\boldsymbol{x}'\right)\underline{\boldsymbol{a}}(d\boldsymbol{x}', d\boldsymbol{\tau}).$$

The minus on the input parameter $\boldsymbol{x}'$ is merely a convention.

B. Wideband Array System Model

A typical digital transmit array architecture will involve digital filtering and (nonadaptive) beamforming followed by digital-to-analog (D/A) conversion and some amount of analog processing (filtering and possibly frequency conversion) prior to the driver (power electronics) and the antenna array itself. We can categorize such architectures into four permutations of two primary design choices. The first is whether to synthesize the radio frequency (RF) signals directly out of the digital-to-analog converters (DACs) or to synthesize first at a lower intermediate frequency (IF) and then use analog upconversion to RF. (Baseband synthesis is also an option in theory but quadrature errors typically preclude it.) The second choice is whether to perform beamforming at baseband or at passband (IF or RF according to the synthesis type). For the purposes of this paper, the specifics of the underlying hardware architecture are largely immaterial, and so we use the simplified passband-equivalent model of Fig. 1. We choose a passband rather than baseband equivalent since propagation is central to the analysis. In this section, the passband-equivalent will be related back to the underlying implementation; in the sequel, the simplified model will be used exclusively with the exception of Section III.

We assume N independent passband-equivalent inputs to the system, represented by the $N \times 1$ vector of real continuous-time signal measures $\underline{\boldsymbol{s}}(dt)$. We will assume that for all architectures

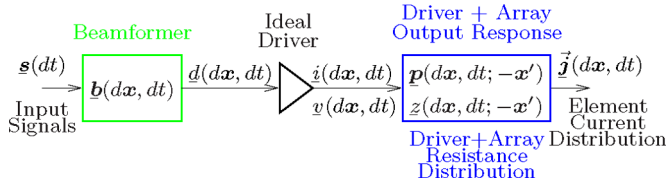

Fig. 1. Passband-equivalent model of transmit beamformer and array.

$\underline{\boldsymbol{s}}$ is derived from a complex discrete-time baseband signal $\underline{\boldsymbol{s}}_{\mathrm{bb}}$ as

$$\underline{\boldsymbol{s}}(dt) = \mathrm{Re}\left\{e^{\mathrm{j}2\pi f_{\mathrm{RF}} t}(\underline{h}_{\mathrm{bb}} * \underline{\boldsymbol{s}}_{\mathrm{bb}})(dt)\right\}$$

where continuous-time low-pass filter $\underline{h}_{\mathrm{bb}}$ represents the cascade of all antialiasing and image-rejection filtering as well as the DAC pulse and any digital filtering to compensate the analog filter effects. We assume this cascade has ideal low-pass transfer function $H_{\mathrm{bb}}(f) \triangleq 1_{\mathcal{F}-f_{\mathrm{RF}}}(f)$, where set $\mathcal{F}$ is the RF signal band and f_{RF} is the nominal RF center frequency. Thus the support of signal spectrum $\boldsymbol{S}$ is $-\mathcal{F} \cup \mathcal{F}$.

Passband-equivalent beamformer response $\underline{\boldsymbol{b}}(d\boldsymbol{x}, dt)$, a $1 \times N$ vector of measures, converts the temporal signals into a scalar space-time signal $\underline{d}(d\boldsymbol{x}, dt)$. The beamformer is discrete-space with the form

$$\underline{\boldsymbol{b}}(d\boldsymbol{x}, dt) = \sum_{\mathbf{x}\in\boldsymbol{\mathcal{L}}} \underline{\boldsymbol{b}}(\mathbf{x}, dt)\,{}_{\mathbf{x}}\underline{\delta}(d\boldsymbol{x})$$

where spatial support $\boldsymbol{\mathcal{L}}$ is the set of element locations in the array. The continuous-time, discrete-space beamformer output $\underline{d}$ represents the drive signals for the elements, and can be written variously as

$$\begin{aligned}\underline{d}(d\boldsymbol{x}, dt) &= (\underline{\boldsymbol{b}} * \underline{\boldsymbol{s}})(d\boldsymbol{x}, dt)\\ &= \sum_{\mathbf{x}\in\boldsymbol{\mathcal{L}}} (\underline{\boldsymbol{b}} * \underline{\boldsymbol{s}})(\mathbf{x}, dt)\,{}_{\mathbf{x}}\underline{\delta}(d\boldsymbol{x})\\ &= \sum_{n=1}^{N}\sum_{\mathbf{x}\in\boldsymbol{\mathcal{L}}} (\underline{b}_n * \underline{s}_n)(\mathbf{x}, dt)\,{}_{\mathbf{x}}\underline{\delta}(d\boldsymbol{x}). \qquad (1)\end{aligned}$$

Scalar filter response $\underline{b}_n(\mathbf{x}, dt)$ maps the nth input signal $\underline{s}_n$ to the output drive signal $\underline{d}(\mathbf{x}, dt)$ at position $\mathbf{x}$.

The mapping of the underlying physical beamformer to the passband equivalent is different for each of the four architecture permutations. The simplest case is passband beamforming followed by RF synthesis, in which case the passband-equivalent beamformer is simply the underlying discrete-time beamformer: $\underline{\boldsymbol{b}}(d\boldsymbol{x}, dt) = \underline{\boldsymbol{b}}_{\mathrm{RF}}(d\boldsymbol{x}, dt)$. For baseband beamforming with RF synthesis, the passband equivalent is still discrete time and is related to the underlying baseband response as

$$\underline{\boldsymbol{b}}(d\boldsymbol{x}, dt) = \mathrm{Re}\left\{e^{\mathrm{j}2\pi f_{\mathrm{RF}} t}(\underline{h}_{\mathrm{int}} * \underline{\boldsymbol{b}}_{\mathrm{bb}})(d\boldsymbol{x}, dt)\right\}$$

where $\underline{h}_{\mathrm{int}}$ is a discrete-time interpolation/image rejection filter. With IF synthesis architectures, the passband equivalent beamformer is continuous time; for baseband beamforming, we have

$$\underline{\boldsymbol{b}}(d\boldsymbol{x}, dt) = \mathrm{Re}\left\{e^{\mathrm{j}2\pi f_{\mathrm{RF}} t}(\underline{h}_{\mathrm{bb}} * \underline{\boldsymbol{b}}_{\mathrm{bb}})(d\boldsymbol{x}, dt)\right\}$$

where $\underline{h}_{\rm bb}$ is as before, and for passband (IF) beamforming we have

$$\underline{\boldsymbol{b}}(d\boldsymbol{x},dt)=\mathrm{Re}\left\{e^{\mathrm{j}2\pi(f_{\rm RF}-f_{\rm IF})t}(\underline{h}_{\rm IF}*\underline{\boldsymbol{b}}_{\rm IF})(d\boldsymbol{x},dt)\right\}$$

where filter $\underline{h}_{\rm IF}$ has transfer function $H_{\rm IF}(f)\triangleq 1_{\mathcal{F}-f_{\rm RF}+f_{\rm IF}}(f)$. For all architectures, the underlying FIR beamformer filter at element location $\mathbf{x}$ has the form

$$\underline{b}'_n(\mathbf{x},dt)=\sum_{\tau\in\mathcal{D}}b'_n(\mathbf{x},\tau)\,{}_\tau\underline{\delta}(dt),$$

where $\underline{b}'_n$ is the nth component of $\underline{\boldsymbol{b}}_{\rm bb}$, $\underline{\boldsymbol{b}}_{\rm IF}$, or $\underline{\boldsymbol{b}}_{\rm RF}$ as appropriate and $\mathcal{D}$ is the set of tap delays. The corresponding temporal Fourier transform reduces to

$$B'_n(\mathbf{x},f)=\sum_{\tau\in\mathcal{D}}b'_n(\mathbf{x},\tau)e^{-\mathrm{j}2\pi f\tau}.$$

Both the physical and passband-equivalent beamformer and their Fourier transforms are linear in the filter coefficients $\{b'_n(\mathbf{x},\tau)\}$, which are real for passband beamforming and complex for baseband beamforming. The real and imaginary components of these coefficients will be implicit optimization variables in the sequel.

Following the beamformer, the ideal driver converts the unitless drive signal into either a drive-current measure $\underline{i}$ or drive-voltage measure $\underline{v}$. Both current and voltage are discrete-space and continuous-time. We will assume current drivers in the sequel, and so we have simply $\underline{i}=\underline{d}$ with an implicit units conversion. The densities of $\underline{i}$ and $\underline{v}$ with respect to counting measure on space and Lebesgue measure on time have units of amps and volts. The ideal driver represents the source in the Norton or Thevenin equivalent circuit for a real driver; the equivalent impedance is merged with the array model for simplicity. The resulting equivalent *resistance distribution* $\underline{z}(d\boldsymbol{x},dt;-\boldsymbol{x}')$ is real-valued with units of Ohms. It provides an LTI, LSV model of the cascade of the nonideal part of the driver, the feed network, and the array as seen by the ideal driver. It relates the drive current and voltage as $\underline{v}=\underline{z}\boxtimes\underline{i}$. As it does not directly affect radiation in this model, further discussion of the resistance distribution will be deferred until Section IV-B.

We are ultimately concerned with the fields radiated by the array, which depend on the currents in the radiating elements of the array. These currents are represented here by the element-current distribution $\vec{\underline{\boldsymbol{j}}}(d\boldsymbol{x},dt)$, a 3×1 field vector (indicated by the overarrow) with units $\mathrm{A}\cdot\mathrm{m}\cdot\mathrm{s}$. The units of the element-current density $\vec{\boldsymbol{j}}$ can be A/m^2, A/m, or Amps, corresponding to reference measures that restrict the current to a volume, surface, or line. The LTI, LSV output response $\underline{\boldsymbol{p}}(d\boldsymbol{x},dt;-\boldsymbol{x}')$, representing the combined responses of the driver, feed network, and array, relates the element-current distribution to the drive current $\underline{i}$. It is related to the impedance distribution, as it completely determines the component of $\underline{z}$ that corresponds to radiation. For our purposes the two responses are considered independently. Like $\vec{\underline{\boldsymbol{j}}},\underline{\boldsymbol{p}}$ has dimension 3×1, and for units consistency $\underline{\boldsymbol{p}}$ has units of meters. The spatial reference measure of $\underline{\boldsymbol{p}}$ is necessarily the same as for $\vec{\underline{\boldsymbol{j}}}$. The element-current distribution is related to the drive current by $\vec{\underline{\boldsymbol{j}}}=\underline{\boldsymbol{p}}\boxtimes\underline{i}$ or, expanding to make the discrete-space nature of the drive current distribution explicit

$$\vec{\underline{\boldsymbol{j}}}(\boldsymbol{\mathcal{X}}\times\mathcal{T})=\sum_{\mathbf{x}'\in\boldsymbol{\mathcal{L}}}\int\underline{\boldsymbol{p}}(\boldsymbol{\mathcal{X}}\times(\mathcal{T}-\tau);-\mathbf{x}')\,\underline{i}(\mathbf{x}',d\tau).\quad(2)$$

Here, we see that the measure $\underline{\boldsymbol{p}}(d\boldsymbol{x},dt;-\mathbf{x}')$ is the spatio-temporal response of the element at location $\mathbf{x}'$ to the corresponding drive current $\underline{i}(\mathbf{x}',dt)$. We can see from (2) that the spatial support $\boldsymbol{\mathcal{L}}$ of the driver current distribution $\underline{i}$ is mathematically somewhat arbitrary, in the sense that $\underline{\boldsymbol{p}}$ can simply be redefined such that an identical element-current distribution $\vec{\underline{\boldsymbol{j}}}$ will result if the spatial support of the drive-current is changed to some other set $\boldsymbol{\mathcal{L}}'$ of K locations. In practice, we usually choose $\boldsymbol{\mathcal{L}}$ to match the physical locations of the element phase centers at some reference frequency, and we will simply refer to $\boldsymbol{\mathcal{L}}$ as the element locations in the sequel. In general the element response at each location can be different, but in the common special case where identical element responses are assumed at each location we have $\underline{\boldsymbol{p}}(\boldsymbol{\mathcal{X}}\times\mathcal{T};-\mathbf{x}')=\underline{\boldsymbol{p}}_0((\boldsymbol{\mathcal{X}}-\mathbf{x}')\times\mathcal{T})$ and $\vec{\underline{\boldsymbol{j}}}=\underline{\boldsymbol{p}}_0\circledast\underline{i}$, where $\underline{\boldsymbol{p}}_0(d\boldsymbol{x},dt)$ is the LTI and LSI element response. Now the choice of $\boldsymbol{\mathcal{L}}$ is not arbitrary, as the offsets between the various locations must match the physical offsets of the elements. An overall spatial shift of $\boldsymbol{\mathcal{L}}$ can still be accommodated through redefinition of $\boldsymbol{p}_0$, however. As we will see, the identical element-response assumption (when it applies) greatly simplifies analysis. Recalling that $\underline{i}=\underline{d}$, substituting (1) into $\vec{\underline{\boldsymbol{j}}}=\underline{\boldsymbol{p}}\boxtimes\underline{i}$ and $\vec{\underline{\boldsymbol{j}}}=\underline{\boldsymbol{p}}_0\circledast\underline{i}$, respectively, and Fourier transforming on $\boldsymbol{x}$ and t to spatial frequency $\boldsymbol{v}$ and temporal frequency f yields

$$\vec{\mathbf{J}}(\boldsymbol{v},f)=\int\mathbf{P}(\boldsymbol{v},f;-\boldsymbol{x}')\underline{\boldsymbol{B}}(d\boldsymbol{x}',f)\boldsymbol{S}(f)\quad(3\mathrm{lsv})$$

$$\vec{\mathbf{J}}(\boldsymbol{v},f)=\mathbf{P}_0(\boldsymbol{v},f)\mathbf{B}(\boldsymbol{v},f)\boldsymbol{S}(f).\quad(3\mathrm{lsi})$$

C. Far-Field Propagation and the Wideband Array Pattern

To compute the far-field array response from the element-current distribution involves solving Maxwell's equations. We take the common approach [29] of solving for the far-field electric field via the magnetic *vector potential*, an intermediate value with a convenient geometric interpretation. This then allows us to define the wideband array pattern, which serves as a transfer function from the array input to the far-field.

1) The Vector Potential: The density of the magnetic vector potential $\vec{\underline{\boldsymbol{\alpha}}}$ is a vector field whose curl is the magnetic field, thus satisfying Gauss' law for magnetism. This does not uniquely specify the vector potential, but it is both customary and convenient to define it as the convolution $\vec{\underline{\boldsymbol{\alpha}}}=(\mu_0/4\pi)(\underline{\rho}\circledast\vec{\underline{\boldsymbol{j}}})$ of the element-current distribution with the propagation measure $\underline{\rho}(d\boldsymbol{x},dt)\triangleq\|\boldsymbol{x}\|^{-1}d\boldsymbol{x}\,{}_{(\|\boldsymbol{x}\|/c)}\underline{\delta}(dt)$. The constants μ_0 and c are the permeability of free space and the propagation speed of light in free space, respectively. The propagation measure is also known as the *retarded Green's function* for free space. The vector potential is the superposition of spherical waves propagating away from each point on the antenna weighted by the element-current density at that point. The shift on the temporal impulse in $\underline{\rho}$ determines the propagation speed, while the $\|\boldsymbol{x}\|^{-1}$ factor sets the scaling with distance required to satisfy the conservation of energy. The vector potential is both continuous-

space and continuous-time, with units of $\mathrm{V}\cdot\mathrm{s}/\mathrm{m}$. Fourier transforming $\underline{\vec{\boldsymbol{\alpha}}}$ on time and writing the result as a density in $\boldsymbol{x}$ yields

$$\vec{\boldsymbol{\mathcal{A}}}(\boldsymbol{x},f)=\frac{\mu_0}{4\pi}\int\frac{e^{-\mathrm{j}2\pi\|\boldsymbol{x}-\boldsymbol{x}'\|f/c}}{\|\boldsymbol{x}-\boldsymbol{x}'\|}\underline{\vec{\boldsymbol{J}}}(d\boldsymbol{x}',f). \tag{4}$$

This expression is nearly identical to a standard textbook result (for example, [29, eq. (3)–(27)] or [30, eq. (7.7)]), with the exceptions that the element-current distribution and vector potential transforms here are conjugate-symmetric, rather than one-sided, functions of temporal frequency, and that the textbook form suppresses explicit frequency dependence in favor of *wavenumber* $k=2\pi f/c=2\pi/\lambda$.

2) The Far-Field Approximation: The vast majority of antenna arrays operate well into the far field, defined here simply as $\|\boldsymbol{x}\|$ "large" relative to the largest array dimension. The essence of the far-field approximation is to expand the norm $\|\boldsymbol{x}-\boldsymbol{x}'\|$ in a two-term Taylor series about $\boldsymbol{x}$: $\|\boldsymbol{x}-\boldsymbol{x}'\|\approx\|\boldsymbol{x}\|-\boldsymbol{x}'\cdot\hat{\boldsymbol{x}}$. Since (4) is a less sensitive function of the norm in the denominator, only the first term will be used there. Substituting yields

$$\vec{\boldsymbol{\mathcal{A}}}(\boldsymbol{x},f)\approx\frac{\mu_0}{4\pi}\frac{e^{-\mathrm{j}2\pi\|\boldsymbol{x}\|f/c}}{\|\boldsymbol{x}\|}\int e^{\mathrm{j}2\pi\boldsymbol{x}'\cdot\hat{\boldsymbol{x}}f/c}\underline{\vec{\boldsymbol{J}}}(d\boldsymbol{x}',f)$$

and recognizing a spatial Fourier transform, we write

$$\vec{\boldsymbol{\mathcal{A}}}(\boldsymbol{x},f)\approx\frac{\mu_0}{4\pi}\frac{e^{-\mathrm{j}2\pi\|\boldsymbol{x}\|f/c}}{\|\boldsymbol{x}\|}\vec{\mathbf{J}}(-\hat{\boldsymbol{x}}f/c,f). \tag{5}$$

This classic and remarkably elegant result says that the far-field vector potential resulting from element-current distribution $\underline{\vec{\boldsymbol{j}}}$ is just a spherical wave (or, locally approximated, a plane wave) weighted in the direction $\hat{\boldsymbol{x}}$ by the spatio-temporal Fourier transform $\mathbf{J}(\boldsymbol{v},f)$ of the element-current distribution evaluated at spatial frequency $\boldsymbol{v}=-\hat{\boldsymbol{x}}f/c$. As a consequence of the far-field assumption, the dependencies on distance $\|\boldsymbol{x}\|$ and direction $\hat{\boldsymbol{x}}$ have been completely decoupled.

3) The Electric Field: The electric field measure is both continuous-space and continuous-time. For reasons of convenience and convention we will operate on its spatial density, and refer to the density throughout as the electric field. The temporal Fourier transform of the electric field at an arbitrary far-field location $\boldsymbol{x}$ is found from the density of the vector potential transform via $\vec{\boldsymbol{\mathcal{E}}}(\boldsymbol{x},f)\approx-\mathrm{j}2\pi f\boldsymbol{\Gamma}_{\hat{\boldsymbol{x}}}\vec{\boldsymbol{\mathcal{A}}}(\boldsymbol{x},f)$ [29]. Matrix $\boldsymbol{\Gamma}_{\hat{\boldsymbol{x}}}\triangleq\mathbf{I}-\hat{\boldsymbol{x}}\hat{\boldsymbol{x}}^T$ projects onto the plane perpendicular to direction vector $\hat{\boldsymbol{x}}$, ensuring that the far-field electric field vector is always oriented perpendicular to the direction of propagation. The electric field transform has units $\mathrm{V}\cdot\mathrm{s}/\mathrm{m}$. Substituting for the vector potential from (5) yields

$$\vec{\boldsymbol{\mathcal{E}}}(\boldsymbol{x},f)\approx-\frac{e^{-\mathrm{j}2\pi\|\boldsymbol{x}\|f/c}}{\|\boldsymbol{x}\|}\frac{\mu_0}{4\pi}\mathrm{j}2\pi f\boldsymbol{\Gamma}_{\hat{\boldsymbol{x}}}\vec{\mathbf{J}}(-\hat{\boldsymbol{x}}f/c,f) \tag{6}$$

the electric field directly as a function of the spatio-temporal Fourier transform of the antenna element-current distribution. Thus, the far-field electric field due to element-current distribution $\underline{\vec{\boldsymbol{j}}}$ is, like the vector potential, a direction-weighted spherical wave, with an additional weighting of $-\mathrm{j}2\pi f$ (a time derivative) and with the radial vector components suppressed.

4) The Wideband Array Pattern: We now return to the system of Fig. 1 and derive the *wideband array pattern*, the effective transfer function from the input signals to the far field. We expand the far-field electric field in terms of the input by substituting (3) into (6)

$$\vec{\boldsymbol{\mathcal{E}}}(\boldsymbol{x},f)\approx-\frac{e^{-\mathrm{j}2\pi\|\boldsymbol{x}\|f/c}}{\|\boldsymbol{x}\|}\frac{\mu_0}{4\pi}\mathrm{j}2\pi f\boldsymbol{\Gamma}_{\hat{\boldsymbol{x}}}\times\int\mathbf{P}(-\hat{\boldsymbol{x}}f/c,f;-\boldsymbol{x}')\underline{\boldsymbol{B}}(d\boldsymbol{x}',f)\boldsymbol{S}(f) \tag{7lsv}$$

$$\vec{\boldsymbol{\mathcal{E}}}(\boldsymbol{x},f)\approx-\frac{e^{-\mathrm{j}2\pi\|\boldsymbol{x}\|f/c}}{\|\boldsymbol{x}\|}\frac{\mu_0}{4\pi}\mathrm{j}2\pi f\boldsymbol{\Gamma}_{\hat{\boldsymbol{x}}}\mathbf{P}_0\times(-\hat{\boldsymbol{x}}f/c,f)\mathbf{B}(\boldsymbol{v},f)\boldsymbol{S}(f). \tag{7lsi}$$

The dependence on distance $\|\boldsymbol{x}\|$ is limited to the spherical-wave factor $e^{-\mathrm{j}2\pi\|\boldsymbol{x}\|f/c}/\|\boldsymbol{x}\|$, with the numerator representing propagation delay and the denominator representing the attenuation of the electric field with distance. Since these are common to all arrays, they are not typically included in the array pattern. The wideband array pattern is the direction-dependent, distance-independent response

$$\vec{\mathbf{A}}(\boldsymbol{v},f)\triangleq-\frac{\mu_0}{4\pi}\mathrm{j}2\pi f\boldsymbol{\Gamma}_{\boldsymbol{v}}\int\mathbf{P}(\boldsymbol{v},f;-\boldsymbol{x}')\underline{\boldsymbol{B}}(d\boldsymbol{x}',f) \tag{8lsv}$$

$$\vec{\mathbf{A}}(\boldsymbol{v},f)\triangleq-\frac{\mu_0}{4\pi}\mathrm{j}2\pi f\boldsymbol{\Gamma}_{\hat{\boldsymbol{v}}}\mathbf{P}_0(\boldsymbol{v},f)\mathbf{B}(\boldsymbol{v},f) \tag{8lsi}$$

which has dimension $3\times N$. Under both the LSV and LSI definitions of the array pattern, the electric field for far-field $\boldsymbol{x}$ reduces to

$$\vec{\boldsymbol{\mathcal{E}}}(\boldsymbol{x},f)\approx\frac{e^{-\mathrm{j}2\pi\|\boldsymbol{x}\|f/c}}{\|\boldsymbol{x}\|}\vec{\mathbf{A}}(-\hat{\boldsymbol{x}}f/c,f)\boldsymbol{S}(f)$$

the product of a spherical wave, the array pattern, and the post-conversion signal spectrum.

The contribution to the array pattern of the elements and the beamformer is seen by defining the *wideband element pattern* for the general (LSV) and identical element (LSI) cases

$$\vec{\mathbf{A}}_{\mathrm{el}}(\boldsymbol{v},f;-\mathbf{x}')\triangleq-\frac{\mu_0}{4\pi}\mathrm{j}2\pi f\boldsymbol{\Gamma}_{\hat{\boldsymbol{v}}}\mathbf{P}(\boldsymbol{v},f;-\mathbf{x}) \tag{9lsv}$$

$$\vec{\mathbf{A}}_{\mathrm{el}}(\boldsymbol{v},f)\triangleq-\frac{\mu_0}{4\pi}\mathrm{j}2\pi f\boldsymbol{\Gamma}_{\hat{\boldsymbol{v}}}\mathbf{P}_0(\boldsymbol{v},f). \tag{9lsi}$$

When all element patterns are identical, then we get the classic array pattern factorization $\vec{\mathbf{A}}(\boldsymbol{v},f)=\vec{\mathbf{A}}_{\mathrm{el}}(\boldsymbol{v},f)\mathbf{B}(\boldsymbol{v},f)$, the product of the element pattern and the *array factor*. It is common under this assumption to design the array factor with minimal knowledge of the element pattern, as array-factor features such as sidelobe levels will largely be preserved in the array pattern. In the general LSV case, however, the element pattern is parametrized on position, allowing each physical element to have a different pattern. The array pattern is then the sum

$$\vec{\mathbf{A}}(\boldsymbol{v},f)=\sum_{\mathbf{x}'\in\boldsymbol{\mathcal{L}}}\vec{\mathbf{A}}_{\mathrm{el}}(\boldsymbol{v},f;-\mathbf{x}')\boldsymbol{B}(\mathbf{x}',f)$$

of the individual element patterns weighted by the frequency responses of the corresponding beamformer subfilters. If $\vec{\mathbf{A}}_{\mathrm{el}}(\boldsymbol{v},f;-\mathbf{x}')$ is the inverse Fourier transform on $\boldsymbol{v}'$ of *bifrequency map* [31] $\breve{\vec{\mathbf{A}}}_{\mathrm{el}}(\boldsymbol{v},f;\boldsymbol{v}')$, then we can write the array pattern in terms of the array factor as

$$\vec{\mathbf{A}}(\boldsymbol{v},f)=\int\breve{\vec{\mathbf{A}}}_{\mathrm{el}}(\boldsymbol{v},f;\boldsymbol{v}')\mathbf{B}(\boldsymbol{v}',f)d\boldsymbol{v}'.$$

Because the bifrequency map can map array-factor spatial frequencies to different array-pattern spatial frequencies, array-factor structure is not preserved in general. In this case, knowledge of the element patterns is necessary for design.

5) Array-Pattern Geometry and the Helmholtz Cone: The preceding derivations reveal two potential spaces in which to visualize the far-field wideband array pattern. One is the restriction of the four-dimensional space of position-frequency pairs $(\boldsymbol{x}, f)$ to the cylindrical shell $\|\boldsymbol{x}\| = 1$, a point on which can equivalently be specified by a direction-frequency pair $(\hat{\boldsymbol{x}}, f)$. Since (8) shows that the wideband array pattern and array factor are spatio-temporal frequency responses, it also seems natural to visualize them in the four-dimensional space of spatial and temporal frequency pairs $(\boldsymbol{v}, f)$. The relationship between these two representations was found in (5) to be $\boldsymbol{v} = -\hat{\boldsymbol{x}} f/c$, which maps the 4-D cylinder defined by $\|\boldsymbol{x}\| = 1$ in $(\boldsymbol{x}, f)$ space to the 4-D cone defined by $\|\boldsymbol{v}\| = |f|/c$ in $(\boldsymbol{v}, f)$ space. From (6), we see that the radiation traveling in the direction $\hat{\mathbf{x}}_0$ looks locally like a plane wave and results from the component of the element-current distribution at spatial frequency $\boldsymbol{v} = -\hat{\mathbf{x}}_0 f/c$. This is a variant of the Helmholtz equation, which describes the conditions for plane-wave propagation. Accordingly, we will refer to the surface $\|\boldsymbol{v}\| = |f|/c$ as the *Helmholtz cone*, and will refer to points on the cone as propagating or "visible" spatio-temporal frequencies. Spatio-temporal frequencies not on the Helmholtz cone, referred to as nonpropagating or "invisible", are effectively filtered out by far-field propagation, and in this way the array acts as a particular kind of spatio-temporal bandpass filter.

Describing and plotting array patterns and array factors in these two geometries presents a challenge. Although the surface $\|\boldsymbol{x}\| = 1$ lies in the 4-D space $(\boldsymbol{x}, f)$, it is really only 3D. We will describe the unit sphere at a given temporal frequency in the spherical coordinate system shown in Fig. 2. Unit-vector $\hat{\boldsymbol{x}}$ can be described by the elevation-azimuth pair (ϕ, θ), and the array pattern can be viewed as a function on the 3-D volume $[-90°, 90°] \times [-180°, 180°] \times \mathbb{R}$ in the space (ϕ, θ, f). When we only wish to visualize one hemisphere of the array pattern (such as with most planar arrays), we can instead project the hemisphere into the bisecting plane. For example, the unit hemisphere in the positive-y halfspace can be projected into the $x-z$ plane and back via the mappings

$$\begin{aligned}\boldsymbol{\Upsilon}(x, y, z) &= (x, z)\\ \boldsymbol{\Upsilon}^{-1}(x, z) &= (x, \sqrt{1 - x^2 - z^2}, z).\end{aligned}$$

The projected hemisphere occupies the unit disk $x^2 + z^2 \leq 1$ in (x, z) space, and the wideband array pattern occupies the solid 3-D cylinder in (x, z, f) space shown in Fig. 3(a). Similar projection approaches can be used to reduce the dimensionality in in terms of spatial frequency. Consider the function pair

$$\begin{aligned}\boldsymbol{\Upsilon}(v_x, v_y, v_z, f) &= (v_x, v_z, f)\\ \boldsymbol{\Upsilon}^{-1}(v_x, v_z, f) &= \left(v_x, -\sqrt{(f/c)^2 - v_x^2 - v_z^2}, v_z, f\right)\end{aligned}$$

that map the half-cone corresponding to negative v_y to $\mathbb{R}^2 \times \mathbb{R}$ and back. At each frequency f the hemispherical shell corresponding to $v_y \leq 0$ is "flattened" to form a disk of radius f/c, and the disks are stacked in frequency to form the classic

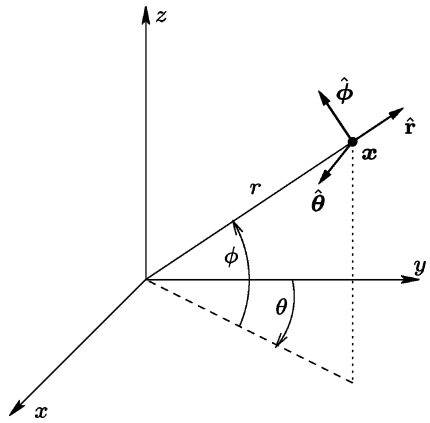

Fig. 2. Spherical coordinate system used to describe antenna array patterns. Elevation angle ϕ is measured up from the horizon (the $x-y$ plane), and azimuth angle θ is measured clockwise from due north (the positive y-axis). Range r is included for completeness. Local Cartesian coordinate system basis vectors $\hat{\boldsymbol{\phi}}$, $\hat{\boldsymbol{\theta}}$, and $\hat{\mathbf{r}}$ indicate the directions of increasing elevation, azimuth, and range, respectively.

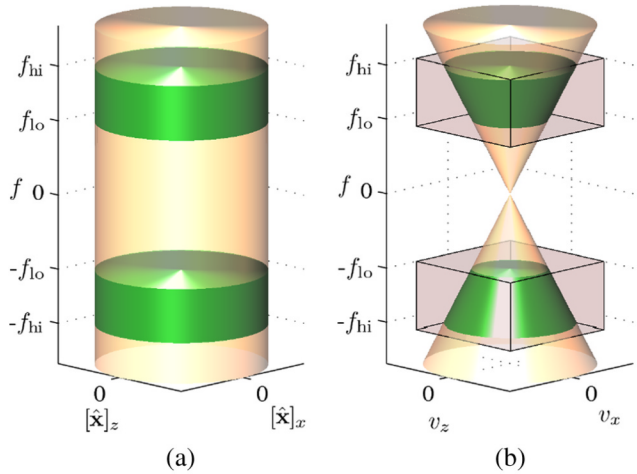

Fig. 3. (a) Projecting the positive-y hemisphere into the $x - z$ plane for each temporal frequency f results in a solid cylinder. The green region represents the signal band. (b) Projecting the negative v_y half of the four-dimensional cone into (v_x, v_z, f) space results in the classic two-sided "ice-cream" cone. The boxes represent one period of the array factor for the example array.

3-D "ice-cream" cone of Fig. 3(b). This solid cone is just a frequency scaled version of the solid cylinder previously derived. This approach is most natural for planar arrays, where the beamformer occupies two spatial dimensions and its corresponding frequency response (the array factor) is thus a function of 2-D spatial frequency. Here, no information is lost in projecting out the third spatial-frequency dimension. For a wideband array whose elements are not confined to a plane, four dimensions are required to fully specify the array factor.

6) Polarization: At a far-field location $\boldsymbol{x}$, the electric field vector of a propagating wave lies in the plane perpendicular to $\boldsymbol{x}$. Often this 2-D subspace is described using the local orthogonal basis vectors $\hat{\boldsymbol{\phi}}(\boldsymbol{x})$ ("vertical") and $\hat{\boldsymbol{\theta}}(\boldsymbol{x})$ ("horizontal"), shown in Fig. 2, which are the (position-dependent) directions of increasing elevation and azimuth, respectively. Arbitrary scalar

fields can then be defined as linear combinations of the horizontal and vertical components

$$\mathcal{E}_{\hat{\boldsymbol{\psi}}}(\boldsymbol{x},f)=\hat{\boldsymbol{\psi}}^H(f)\begin{pmatrix}\hat{\boldsymbol{\phi}}^T(\boldsymbol{x})\\ \hat{\boldsymbol{\theta}}^T(\boldsymbol{x})\end{pmatrix}\vec{\boldsymbol{\mathcal{E}}}(\boldsymbol{x},f) \tag{10}$$

where 2×1 complex unit vector $\hat{\boldsymbol{\psi}}$ is a wideband extension of the *Jones vector* [32] often used to describe narrowband polarization. Wideband Jones vectors for common polarization types include $\binom{1}{0}$ (vertical), $\binom{0}{1}$ (horizontal), $\binom{1}{\mathcal{H}(f)}/\sqrt{2}$ (right-hand circular), and $\binom{1}{-\mathcal{H}(f)}/\sqrt{2}$ (left-hand circular), where $\mathcal{H}(f)\triangleq -\mathrm{jsgn}(f)$ is the frequency response of the Hilbert transformer. The Hilbert preserves conjugate symmetry, as $\vec{\boldsymbol{\mathcal{E}}}$ is the Fourier transform of a real signal. The nth column of the array pattern (corresponding to the nth input signal) can also be decomposed into horizontal and vertical polarization components $\vec{\mathbf{A}}_n(\boldsymbol{v},f)=\mathrm{A}_{n\mathrm{V}}(\boldsymbol{v},f)\hat{\boldsymbol{\phi}}(-\boldsymbol{v})+\mathrm{A}_{n\mathrm{H}}(\boldsymbol{v},f)\vec{\boldsymbol{\theta}}(-\boldsymbol{v})$, although the decomposition is only meaningful for propagating spatial frequencies $\boldsymbol{v}=-\hat{\boldsymbol{x}}f/c$. The polarization of an array pattern is a linear combination of the polarizations of its elements, and thus an array with identical element responses permits no control over the polarization. The array polarization in this case will be that of the common element pattern

$$\begin{aligned}\vec{\mathbf{A}}_n(\boldsymbol{v},f)&=\vec{\mathbf{A}}_{\mathrm{el}}(\boldsymbol{v},f)\mathrm{B}_n(\boldsymbol{v},f)\\ &=\Big[\mathrm{A}_{\mathrm{elV}}(\boldsymbol{v},f)\hat{\boldsymbol{\phi}}(-\boldsymbol{v})+\mathrm{A}_{\mathrm{elH}}(\boldsymbol{v},f)\hat{\boldsymbol{\theta}}(-\boldsymbol{v})\Big]\,\mathrm{B}_n(\boldsymbol{v},f).\end{aligned}$$

Two or more sets of elements with differing polarizations permit polarization control; typically, these would be co-located in pairs (or triples, etc.) or arranged in offset lattices as in [21].

III. Example Design Setup

A common architecture will be used throughout the next section for a series of incremental example designs that allow for direct comparisons between various designs. For pattern-design purposes much of the underlying architectural details are irrelevant; the necessary details are summarized in this section. An IF synthesis architecture will be assumed, which has the advantage of decoupling the RF from the DAC sampling rate. In our examples we will design the array pattern for a single signal ($N=1$). The underlying scalar IF beamformer $\underline{b}_{\mathrm{IF}}$ that was defined in Section II-B is composed of subfilters $\underline{b}_{\mathrm{IF}}(\mathbf{x},dt)$ at each element location $\mathbf{x}$. Each is here an FIR filter with 16 real coefficients located symmetrically about the origin with spacing T. (If the beamformer was instead operated at baseband, roughly equivalent performance would result from an FIR filter with eight complex coefficients at a spacing of $2T$.) This beamformer, operating at a rate $f_s=1/T$, produces a digital IF signal of bandwidth $0.4f_s$ centered at $f_{\mathrm{IF}}=0.25f_s$ which is converted to analog and frequency-converted to a nominal transmit center frequency of $f_{\mathrm{RF}}=0.75f_s$. The passband-equivalent beamformer $\underline{b}$, then, is related to the underlying IF beamformer by $\underline{B}(d\boldsymbol{x},f)=\underline{B}_{\mathrm{IF}}(d\boldsymbol{x},f-f_{\mathrm{RF}}+f_{\mathrm{IF}})$ for signal-band frequencies $f\in\mathcal{F}=[0.55f_s,0.95f_s]$. This defines the IF beamformer on $[0.05f_s,0.45f_s]$, and what remains undefined over the interval $[-0.5f_s,0.5f_s]$ after conjugate symmetry is taken into account is available for transition bands. We note in passing that f_{RF} was chosen primarily to achieve a moderately high ratio of bandwidth to RF; it also happens to lie at the center of the second Nyquist band, and could be synthesized directly out of the DAC by use of an appropriate bandpass reconstruction filter. The proximity of the upper band edge to the first null of the typical zero-order hold response might make this impractical, however.

The example array consists of elements on a square (offset) lattice in the $x-z$ plane, 16 elements wide along the x-axis and seven elements high along the z-axis, symmetrically located about the origin. Array normal is thus the y-axis. The inter-element spacing $d=c/(2\times 0.95f_s)$ is one-half wavelength at the highest frequency of operation, a common choice. The array factor is independently periodic in spatial frequency components v_x and v_z, and is constant in v_y. It is completely defined by its value on the set of spatial frequencies $[-1/2d,1/2d]\times\{0\}\times[-1/2d,1/2d]$, which we will hereafter refer to simply as a spatial frequency period of the array factor. By the given choice of d, at $f=0.95f_s$ the projection of the Helmholtz cone onto the (v_x,v_z) plane exactly inscribes this array factor period, eliminating grating lobes at all temporal frequencies. The pair of boxes in Fig. 3(b) show the resulting region of design control $[-1/2d,1/2d]\times[-1/2d,1/2d]\times([0.5f_s,f_s]\cup[-f_s,-0.5f_s])$ in (v_x,v_z,f) space.

The array elements are identical short vertical ($\hat{\mathbf{z}}$-oriented) dipoles of length $\lambda_{\mathrm{RF}}/20$ located a distance h in front of a perfect ground in the $x-z$ plane; h is a quarter-wavelength at the geometric band center $f_0=\sqrt{0.55f_s\times 0.95f_s}\approx 0.72f_s$. The corresponding element pattern for $|\theta|\le 90^\circ$ is [29]

$$\begin{aligned}\vec{\mathbf{A}}_{\mathrm{el}}(-\hat{\boldsymbol{x}}f/c,f)&\approx-\frac{\mu_0}{4\pi}2\pi fL\sin\left(2\pi h\cos(\phi)\cos(\theta)f/c\right)\\ &\quad\times\cos(\phi)\hat{\boldsymbol{\phi}}(\hat{\boldsymbol{x}})\\ &=\mathrm{A}_{\mathrm{elV}}(-\hat{\boldsymbol{x}}f/c,f)\hat{\boldsymbol{\phi}}(\hat{\boldsymbol{x}})\end{aligned} \tag{11}$$

(the dependence of ϕ and θ on $\hat{\boldsymbol{x}}$ is suppressed), various slices of which are shown in Fig. 4. Due to symmetry, the element pattern is purely real. Short dipoles were chosen here because their element pattern is easy to derive and they are relatively wideband and omnidirectional over a hemisphere. They do not, in most cases, represent a good choice for practical designs because their small size leads to low radiation resistance. Indeed, we will see later that even a small series loss resistance in the element or its feed can have a significant effect on the efficiency of an array of small dipoles. Since all elements have identical responses, the array pattern factors as $\vec{\mathbf{A}}(\boldsymbol{v},f)=\vec{\mathbf{A}}_{\mathrm{el}}(\boldsymbol{v},f)\mathrm{B}(\boldsymbol{v},f)$, and thus imposing even symmetry $b(-\boldsymbol{x},-t)=b(\boldsymbol{x},t)$ on the (real) beamformer (or equivalently on b_{IF}) ensures that the array factor and the overall array pattern are purely real also. This restriction reduces by half the number of independent optimization variables and simplifies certain constraints. We can simplify notation in the examples by using the factorization in (11) to write the visible array pattern as $\vec{\mathbf{A}}(-\hat{\boldsymbol{x}}f/c,f)=\mathrm{A}_{\mathrm{elV}}(-\hat{\boldsymbol{x}}f/c,f)\hat{\boldsymbol{\phi}}(\hat{\boldsymbol{x}})\mathrm{B}(-\hat{\boldsymbol{x}}f/c,f)$, as the unit vector will fall out of most expressions.

In a conventional narrowband or wideband array design, a prototype array pattern is designed to point to boresight, and then that prototype is used to generate patterns pointing in all other directions by applying direction-dependent phase shifts (narrowband) or time delays (wideband) to the signal entering each element. The result is a family of array patterns that at each temporal frequency are simply spatial-frequency-shifted

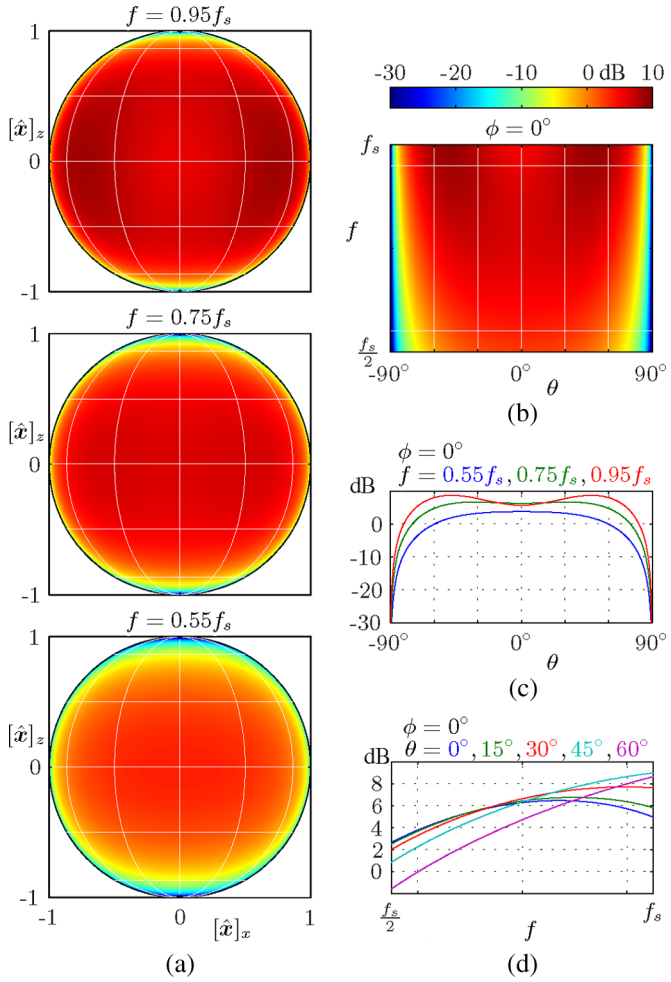

Fig. 4. Pattern of a short vertical dipole in front of a ground plane. (a) Element pattern directive gain. (b) Element pattern slice at $\phi = 0°$. (c) Angular response detail. (d) Frequency response detail.

copies of the prototype. While this is a computationally efficient approach, it precludes performing truly optimal designs for each beam-center direction. The approach advocated here is to optimize a custom array pattern for each beam-center direction, and thus a non-boresight beam-center direction of $\hat{\mathbf{x}}_0 = (1/\sqrt{2})\begin{pmatrix}1\\1\\0\end{pmatrix}$ is used for all example designs as a typical example of one of many related designs. In polar coordinates this is elevation $\phi = 0°$ and azimuth $\theta = 45°$. A further difference from narrowband design is that we have to define a desired value $\mathrm{A}_0(f)$ of the scalar frequency response $\mathrm{A}_\mathrm{V}(-\hat{\mathbf{x}}_0 f/c, f)$ of the array in the nominal beam direction. Two obvious candidates stand out: $\mathrm{A}_0(f) = 1$ and $\mathrm{A}_0(f) = \mathrm{A}_\mathrm{elV}(-\hat{\mathbf{x}}_0 f/c, f)$. The latter is the traditional choice which maintains the element-pattern frequency response, while the former (used in the examples) uses the array factor to flatten the frequency response. Frequency-response constraints are considered further in Section IV-E.

IV. Array Pattern Synthesis

The preceding sections focused on the analysis of wideband transmit arrays, tracing signals from input to far-field electric field. Now we consider synthesis: to control the electric field through design of the array pattern. In this section we will derive performance metrics for the array pattern and show that efficient numerical optimization can be used for design. These metrics largely concern the transfer of power, resulting in expressions that are quadratic in the beamformer coefficients. A natural optimization framework for such problems is second-order cone programming [33] (SOCP), which can optimize objectives that are linear in the optimization variables (here, the beamformer coefficients) subject to linear and convex quadratic constraints. We do not here address the mathematical details of converting FIR-filter and array-pattern optimization problems into canonical SOCP form; for that the interested reader is referred to [1], [10], [34], [35]. Several example designs of the array described in the previous section will be interspersed with the derivations.

A. Far-Field Power Intensity and Directivity

Traditional electromagnetics texts often assume narrowband inputs and derive power metrics accordingly. Here we derive extensions to the traditional radiation power intensity, directive gain, and directivity (given in [29], for example) to describe the distribution of power across both direction and temporal frequency. The analysis here is restricted to finite-duration/energy deterministic waveforms, but the results extend cleanly to time-stationary random processes [22].

For a deterministic input waveform of finite duration T_s the *average radiation power intensity* at far-field position $\boldsymbol{x}$ can be computed in either the time or frequency domain as

$$\mathcal{U}_\mathrm{avg}(\boldsymbol{x}) = \int \frac{||\boldsymbol{x}||^2}{\eta T_s} ||\vec{\boldsymbol{\mathcal{E}}}(\boldsymbol{x}, t)||^2 \, dt = \int \frac{||\boldsymbol{x}||^2}{\eta T_s} \left|\left|\vec{\boldsymbol{\mathcal{E}}}(\boldsymbol{x}, f)\right|\right|^2 df$$

where η is the impedance of free space. The factor of $||\boldsymbol{x}||^2$ cancels the inverse-square dependence of $||\vec{\boldsymbol{\mathcal{E}}}||^2$ on distance, resulting in units of W/sr, where steradian sr is a unit of solid angle. We will define the integrand of the frequency-domain integral as the *radiation power spectral intensity* $\mathcal{U}(\boldsymbol{x}, f)$, with units $\mathrm{W/Hz \cdot sr}$. Writing $\mathcal{U}$ in terms of the array pattern for a single input yields

$$\mathcal{U}(\boldsymbol{x}, f) = \frac{1}{\eta} \left|\left|\vec{\mathbf{A}}(-\hat{\boldsymbol{x}} f/c, f)\right|\right|^2 \frac{1}{T_s} |S(f)|^2 \qquad (12)$$

confirming that the intensity is not a function of distance. To find the total time-average radiated power in all directions and frequencies, we integrate $\mathcal{U}$ over the unit sphere and temporal frequency

$$\mathcal{P}_\mathrm{rad} = \int \int \mathcal{U}(\boldsymbol{x}, f) \underline{\Omega}(d\boldsymbol{x}) df \qquad (13)$$

where $\underline{\Omega}$ is the surface-area measure on the unit sphere with total measure 4π steradians. Power in a particular set of directions of frequencies is found via appropriate integral limits in (13).

Narrowband *directive gain* in a given direction and frequency is defined as the ratio of the radiation power intensity of the antenna to that of an isotropic antenna radiating the same total power. It represents a frequency-dependent normalization of the array pattern, which is generally undesirable in a wideband setting. Narrowband *directivity* is defined as the maximum value of the directive gain, and thus is also frequency dependent. Narrowband directivity is a measure of how well an antenna can focus far-field radiation at a particular frequency. For wideband

systems, we seek a frequency-independent normalization to define directive gain and directivity. Let $\mathcal{F}$ be the spectral support of the input signal. Then we will define the *wideband directive gain* over the frequency band $\mathcal{F}$ as the ratio of the power intensity to the intensity that would result if the same amount of power were instead radiated uniformly over $\mathcal{F}$ from an isotropic antenna

$$\mathcal{D}(\boldsymbol{x}, f) \triangleq \frac{\mathcal{U}(\boldsymbol{x}, f)}{\frac{1}{4\pi \int_{\mathcal{F}} df} \mathcal{P}_{\mathrm{rad}}}.$$

This normalization, while frequency-independent, is input-signal dependent. In order to remove signal dependence we assume an idealized single input with unit average power and a brickwall spectrum $|S(f)|^2 = T_s 1_{\mathcal{F}}(f) / \int_{\mathcal{F}} df$ on the signal band $\mathcal{F}$. Now the directive gain reduces to a function of the array pattern only

$$\mathcal{D}(\boldsymbol{x}, f) = \frac{\|\vec{\mathbf{A}}(-\hat{\boldsymbol{x}} f/c, f)\|^2}{\frac{1}{4\pi \int_{\mathcal{F}} df} \int_{\mathcal{F}} \int \|\vec{\mathbf{A}}(-\hat{\boldsymbol{x}} f/c, f)\|^2 \underline{\Omega}(d\boldsymbol{x}) df} \tag{14}$$

a definition introduced in [11]. It provides a convenient way to normalize various antenna patterns for comparison purposes, and will be used throughout the examples to come. *Wideband directivity* is found by averaging the wideband directive gain across frequency and maximizing over direction

$$\mathcal{D}_0 \triangleq \frac{1}{\int_{\mathcal{F}} df} \int_{\mathcal{F}} \mathcal{D}(\hat{\boldsymbol{x}}_0, f) df = \frac{4\pi}{\mathcal{P}_{\mathrm{rad}}} \int_{\mathcal{F}} \mathcal{U}(\hat{\boldsymbol{x}}_0, f) df \tag{15}$$

where $\hat{\boldsymbol{x}}_0$ is the direction of maximum average directive gain. Substituting (14) into (15) yields

$$\mathcal{D}_0 = \frac{\int_{\mathcal{F}} \|\vec{\mathbf{A}}(-\hat{\boldsymbol{x}}_0 f/c, f)\|^2 df}{\frac{1}{4\pi} \int_{\mathcal{F}} \int \|\vec{\mathbf{A}}(-\hat{\boldsymbol{x}} f/c, f)\|^2 \underline{\Omega}(d\boldsymbol{x}) df} \tag{16}$$

a signal-independent definition of wideband directivity. Wideband directivity provides a metric which we might wish to maximize in a design. Top and bottom are each convex quadratic functions of the beamformer coefficients, but with SOCP we cannot directly optimize the ratio. Instead, we will effectively fix the numerator and minimize the denominator, as demonstrated in the following example.

1) Example: Maximizing Wideband Directivity: For a first example design, we will maximize the wideband directivity by solving the following SOCP problem

$$\min. \quad \alpha > 0 \tag{17a}$$

$$\text{s.t.} \quad \int_{\mathcal{F}} \int |\mathrm{A_V}(-\hat{\boldsymbol{x}} f/c, f)|^2 \underline{\Omega}(d\boldsymbol{x}) df \leq \alpha^2 \tag{17b}$$

$$\frac{1}{\int_{\mathcal{F}} df} \int_{\mathcal{F}} |\mathrm{A_V}(-\hat{\mathbf{x}}_0 f/c, f) - \mathrm{A_0}(f)|^2 df \leq 10^{-\frac{40}{10}}. \tag{17c}$$

The objective and constraint of (17b) together serve to minimize the denominator of (16); auxiliary optimization variable α is used because SOCP requires a linear objective. Mainbeam passband constraint (17c) limits the mean-square difference across the passband $\mathcal{F}$ between the array pattern in the steering direction $\mathbf{x}_0$ and the desired response (in this case, unity) to -40 dB. This effectively fixes the numerator of (16), and thus the result is to maximize wideband directivity.

The problem was setup using a custom Matlab toolbox [1], which passes a canonical SOCP to one of several available solvers [2]–[4]. The integral in (17b) was approximated using a weighted Riemann sum over a dense grid of spatio-temporal frequencies. The result was a single, full-rank quadratic represented as a SOC constraint. Likewise, the integral in (17c) was approximated using a Riemann sum over a dense grid of temporal frequencies, resulting in a second SOC constraint. Since it was formed from responses on a single line through the array pattern, this SOC constraint was of much less than full rank. Total problem setup time on a 1.6 GHz Pentium-M laptop took 465 s, and solving took another 445 s. The optimal wideband directivity was found to be 24.3 dB, and the resulting optimal array pattern and array factor are shown in Fig. 5. Fig. 5(a) shows the wideband directive gain of the optimal array pattern over the entire visible hemisphere of look directions $\hat{\boldsymbol{x}}$, projected onto the $x-z$ plane, for temporal frequencies at the band edges and the band center. The horizontal lines indicate constant elevation angle, while the vertical curved lines indicate constant azimuth angle, both in increments of 30°. Fig. 5(c) also shows the array pattern, this time a slice across temporal frequency and azimuth angle at zero elevation, while Fig. 5(e) and (f) show selected one-dimensional details. A notable feature seen in these plots is that the angular resolution of the array pattern is very nearly constant across temporal frequency. Fig. 5(b) shows one spatial-frequency period of the array factor at the same temporal frequencies as Fig. 5(a), with the white circles indicating the Helmholtz cone boundary. Similarly, Fig. 5(d) shows a slice across temporal frequency and spatial-frequency component v_x at $v_z = 0$, with the diagonal white lines indicating the Helmholtz boundary. The array factor has been normalized so that the wideband directive gain of the array pattern is the product of the wideband directive gain of the element pattern and the array factor. Inside the Helmholtz cone, the array factor is well behaved, and we can see that because of the temporal-frequency-dependent relationship between direction and spatial frequency, the spatial-frequency resolution of the array factor must be greater at lower temporal frequencies than at higher ones to maintain constant angular resolution in the array pattern. Outside the Helmholtz cone, however, the array factor grows extremely large, exceeding 100 dB (the plots are clipped to retain detail within the cone). These huge "invisible" sidelobes are most prominent at lower temporal frequencies, where there is a larger transition zone between the cone in the displayed spatial-frequency period and the adjacent ones. This type of result is often seen in filter optimization problems where a large spectral region is left unconstrained, and here we have no constraints that directly affect the invisible sidelobes. If we were to measure the narrowband directivity of the array pattern at the lower band edge, we would find that it slightly exceeded (by 1–2 dB) the classical textbook directivity limit for an array of this size at that frequency. We say this array pattern exhibits *superdirectivity*, a topic which is very well covered in the literature. (Early work includes [36]–[38] and [11] and [39] provide further references.) Most of the work on superdirectivity has concluded (properly) that it leads to

impractical designs; mitigating the harmful side-effects is a recurring theme in the study of narrowband array-pattern optimization [40]–[42]. These side-effects include extremely low efficiency and extremely high sensitivity to hardware errors. In the following sections, we consider these additional metrics as they apply to wideband arrays.

B. Input Power and Efficiency

Having accounted for power radiated from the array, we now wish to return to the system model of Fig. 1 and focus on the voltage/current relationship at the ideal-driver output in order to determine the power flowing into the array. We will then derive metrics such as efficiency and gain that depend in part on power transfer from the active circuit (drivers) to the array. Such constraints are essential in the design of practical wideband arrays to avoid superdirectivity.

Since both voltage and current have spatial support on the discrete set $\boldsymbol{\mathcal{L}}$, $\underline{z}$ necessarily has the form

$$\underline{z}(d\boldsymbol{x}, dt; -\boldsymbol{x}') = \sum_{\mathbf{x}\in\boldsymbol{\mathcal{L}}} \underline{z}(\mathbf{x}, dt; -\boldsymbol{x}')\,{}_{\mathbf{x}}\underline{\delta}(d\boldsymbol{x}).$$

The temporal Fourier transform $\underline{Z}(d\boldsymbol{x}, f; -\boldsymbol{x}')$ of the resistance distribution is the *impedance measure*, which also has units of Ohms but is complex valued in general. The impedance measure is the measure-system equivalent to a two-sided frequency-dependent impedance matrix, as can be seen by manipulating its defining relation

$$\begin{aligned}\underline{V}(d\boldsymbol{x}, f) &= (\underline{Z}\square\underline{I})(d\boldsymbol{x}, f)\\ &= \sum_{\mathbf{x},\mathbf{x}'\in\boldsymbol{\mathcal{L}}} Z(\mathbf{x}, f; -\mathbf{x}')I(\mathbf{x}', f)\,{}_{\mathbf{x}}\underline{\delta}(d\boldsymbol{x}). \quad (18)\end{aligned}$$

The density of the voltage measure at each location $\mathbf{x}$ is just the weighted sum of the density of the current measure at all locations $\mathbf{x}' \in \boldsymbol{\mathcal{L}}$ through the frequency responses $\{Z(\mathbf{x}, f; -\mathbf{x}')\}$: a $K \times K$ matrix multiply, where K is the number of elements. We will assume that the circuit is reciprocal, so that the impedance density obeys the symmetry relationship $Z(\mathbf{x}, f; -\mathbf{x}') = Z(\mathbf{x}', f; -\mathbf{x})$.

The average input power delivered to the array by the ideal driver over the signal duration T_s is found by integrating the product of the current and voltage over space and either time or frequency

$$\mathcal{P}_{\text{in}} = \frac{1}{T_s}\int i(\boldsymbol{x}, t)\underline{v}(d\boldsymbol{x}, dt) = \frac{1}{T_s}\int I^*(\boldsymbol{x}, f)\underline{V}(d\boldsymbol{x}, f)df.$$

Since $\mathcal{P}_{\text{in}}$ is real, substituting (18) and using the symmetry of Z yields

$$\mathcal{P}_{\text{in}} = \frac{1}{T_s}\int \sum_{\mathbf{x},\mathbf{x}'\in\boldsymbol{\mathcal{L}}} I^*(\mathbf{x}, f)\,\text{Re}\left\{Z(\mathbf{x}, f; -\mathbf{x}')\right\} I(\mathbf{x}', f)df. \quad (19)$$

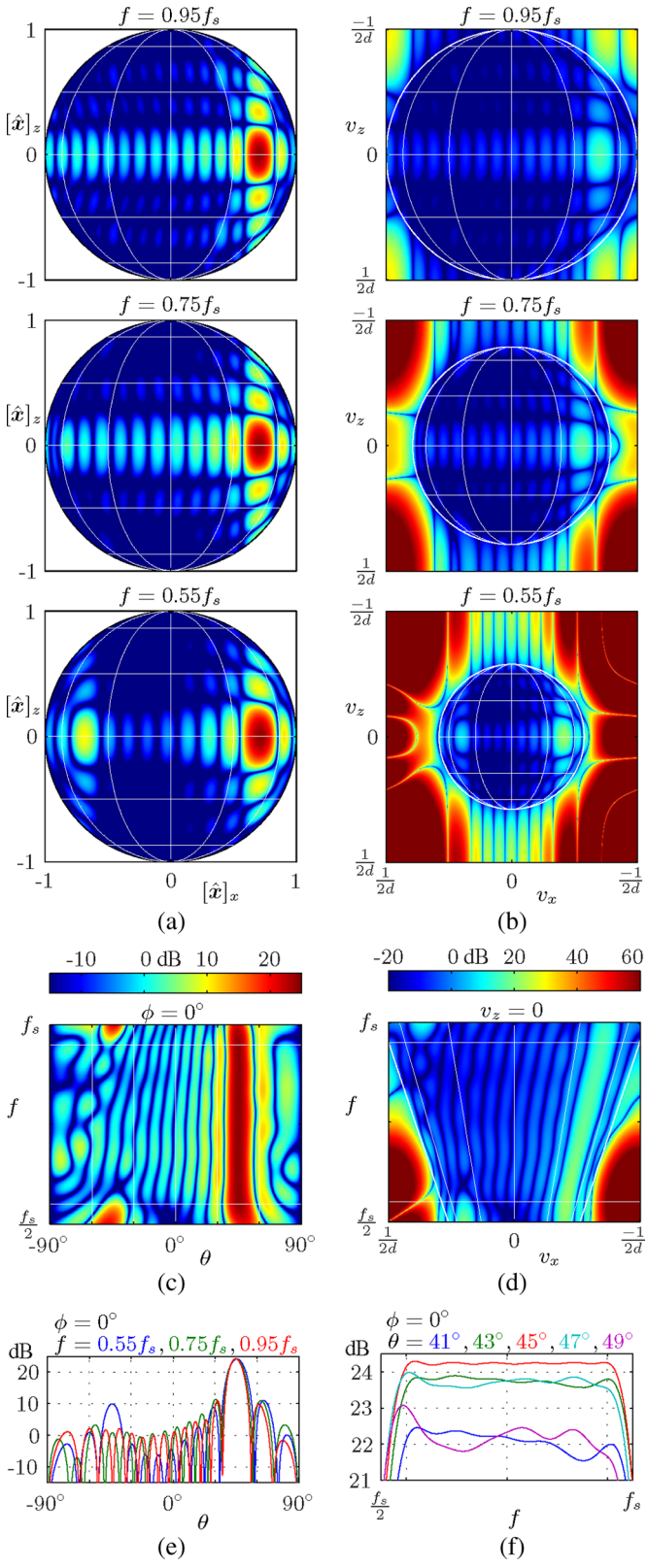

Fig. 5. Results of maximizing directivity. (a) Array pattern directive gain. (b) Array factor. (c) Array pattern slice at $\phi = 0°$. (d) Array factor slice $v_z = 0$. (e) Array response detail. (f) Frequency response detail.

The input power thus depends only on the real part of the impedance, a multidimensional restatement of a first-year cir-

cuits result: reactive elements consume no real power. Finally, Fourier transforming (1) and substituting into (19) yields

$$\mathcal{P}_{\text{in}} = \frac{1}{T_s}\int \sum_{\mathbf{x},\mathbf{x}'\in\boldsymbol{\mathcal{L}}} \boldsymbol{B}^*(\mathbf{x},f)\boldsymbol{S}^*(f)\text{Re}\left\{Z(\mathbf{x},f;-\mathbf{x}')\right\} \times \boldsymbol{S}^T(f)\boldsymbol{B}^T(\mathbf{x}',f)df \quad (20)$$

the input power as a function of the converted input signal and beamformer. This expression is quadratic in the underlying beamformer coefficients. Since Z represents a passive system, quadratic $\mathcal{P}_{\text{in}}$ is necessarily nonnegative and thus convex.

The power input to the array is either radiated or is lost as heat in the driver circuits, feed network, or elements. Thus we can trivially write $\mathcal{P}_{\text{in}} = \mathcal{P}_{\text{rad}} + \mathcal{P}_{\text{loss}}$. In some cases we can derive $\mathcal{P}_{\text{loss}}$ directly without knowledge of the impedance measure, which can be difficult to compute. Consider an array of identical electrically small elements driven by our ideal current source. If the sources and array are ideal, then the equivalent impedance Z seen by the current drivers is just Z_{rad}, the radiation impedance of the array, and since no power is lost in the source or array we have $\mathcal{P}_{\text{in}} = \mathcal{P}_{\text{rad}}$. Of course, in a real array, losses are inevitable. Unless superconducting elements and feeds are used [43], the array will have series resistive losses. If Z_0 is the series loss resistance of one element, then the equivalent circuit impedance is now $Z = Z_{\text{rad}} + Z_{\text{loss}}$, where (ignoring all other sources of loss) $Z_{\text{loss}}(\boldsymbol{x},f;-\boldsymbol{x}') = Z_0$ for $\boldsymbol{x} = \boldsymbol{x}'$, and 0 otherwise. Now the input power is

$$\begin{aligned}\mathcal{P}_{\text{in}} &= \frac{1}{T_s}\int \sum_{\mathbf{x},\mathbf{x}'\in\boldsymbol{\mathcal{L}}} I^*(\mathbf{x},f)\text{Re}\left\{Z_{\text{rad}}(\mathbf{x},f;-\mathbf{x}')\right\} I(\mathbf{x}',f)df \\ &\quad + \frac{Z_0}{T_s}\int \sum_{\mathbf{x}\in\boldsymbol{\mathcal{L}}} |I(\mathbf{x},f)|^2\, df \\ &= \mathcal{P}_{\text{rad}} + \mathcal{P}_{\text{loss}}.\end{aligned}$$

Expanding $\mathcal{P}_{\text{loss}}$ for a single input yields

$$\mathcal{P}_{\text{loss}} = \frac{Z_0}{T_s}\int |S(f)|^2 \sum_{\mathbf{x}\in\boldsymbol{\mathcal{L}}} |B(\mathbf{x},f)|^2\, df \quad (21)$$

a spectrally weighted integral of the sum of the magnitude-squared frequency responses of all the component filters in the beamformer. Applying a variant of Parseval's relation based on the multidimensional Bohr transform [44], [45] to (21) yields

$$\mathcal{P}_{\text{loss}} = \left\langle \frac{Z_0}{T_s}\int |S(f)|^2 \left|\text{B}(\boldsymbol{v},f)\right|^2 df \right\rangle_{\boldsymbol{v}}$$

where $\langle\cdot\rangle_{\boldsymbol{v}}$ indicates averaging over $\boldsymbol{v}$. This result, which holds both when B is periodic ($\boldsymbol{\mathcal{L}}$ lies on a lattice) and when it is almost periodic (arbitrary $\boldsymbol{\mathcal{L}}$), shows that the power lost to resistive heating is equally dependent on the array factor over all spatial frequencies. In contrast, from (8lsi) and (12) we see that for arrays with identical element responses the radiated power depends on the array pattern (and thus the array factor) only for spatio-temporal frequencies on the Helmholtz cone. Thus we expect large values of the array factor off the cone to lead to large power losses, without corresponding increases in transmitted power. The result is poor efficiency.

Traditionally, antenna efficiency is defined as the ratio of the total power "accepted by the antenna from a connected transmitter" [29] to the total power radiated, thus not including the efficiency of the transmitter itself. Since our simple model does not cleanly separate the transmitter and the antenna, we will define the efficiency of an array as the ratio of radiated power to driver input power

$$\xi = \frac{\mathcal{P}_{\text{rad}}}{\mathcal{P}_{\text{in}}} = \frac{\mathcal{P}_{\text{rad}}}{\mathcal{P}_{\text{rad}} + \mathcal{P}_{\text{loss}}}. \quad (22)$$

This definition might include driver losses not included in the classical definition. If we return to the example design of Section IV-A1, we see that the array factor has extremely large values outside of the Helmholtz cone, and thus we suspect that efficiency will be poor with nonzero element series loss resistance. If we assume that the series resistance of a single small dipole is $Z_0 = 0.1\ \Omega$ (for the sake of comparison, the radiation resistance of a single isolated small dipole with the given dimensions at the nominal signal frequency is approximately 1 Ω), and that the input signal has a flat bandlimited spectrum $|S(f)|^2 = T_s 1_{\mathcal{F}}(f)/\int_{\mathcal{F}} df$ as before, then we find that the efficiency of the example design is a vanishingly small $\xi = 9.3\cdot 10^{-8}$. Essentially all input power is lost as heat. Physically, the currents going into each element are extremely large but with alternating polarity in adjacent elements. This results primarily in cancellation in the far field, and little radiated power.

1) Example: Maximizing Efficiency: Clearly, optimizing wideband directivity alone leads to impractical designs. Given the low efficiency that resulted from maximizing wideband directivity, we might wish to maximize efficiency instead. Like wideband directivity, efficiency is a ratio of quadratics, but in this case we cannot directly fix the numerator. Instead, we minimize $\mathcal{P}_{\text{loss}}$ by solving the following SOC program:

$$\begin{aligned}&\min. \quad \alpha > 0 && (23a)\\ &\text{s.t.} \quad \int_{\mathcal{F}} \sum_{\mathbf{x}\in\boldsymbol{\mathcal{L}}} |B(\mathbf{x},f)|^2\, df \le \alpha^2 && (23b)\\ &\quad \frac{1}{\int_{\mathcal{F}} df}\int_{\mathcal{F}} |\text{A}_{\text{V}}(-\hat{\mathbf{x}}_0 f/c,f) - \text{A}_0(f)|^2\, df \le 10^{-\frac{40}{10}}. && (23c)\end{aligned}$$

The objective and SOC constraint (23b) together minimize the power lost to heating. The mainbeam passband constraint (23c) is exactly as in the previous design. Here, it serves to effectively lower bound the radiated power $\mathcal{P}_{\text{rad}}$, so that by (22) minimizing $\mathcal{P}_{\text{loss}}$ maximizes efficiency. Interestingly, although the value of Z_0 is critical to the actual value of the lost power, it is irrelevant as far as the optimization is concerned. All integrals are again computed as Riemann sums over sets of discrete frequencies. Total setup time for this example was 30 s, while the solver took less than 1 s by taking advantage of the sparse internal representation of the SOC constraint (23b). Assuming as before that $Z_0 = 0.1\ \Omega$, the optimal efficiency was found to be 94%, and the corresponding wideband directivity is 22.2 dB, or 2.1 dB less than the previous design. The resulting array pattern and array factor are shown in Fig. 6. Examining the array factor, we can see that the huge invisible sidelobes are gone, and that the sidelobes are continuous across the Helmholtz boundary. This provides visual confirmation that (23b) has indeed constrained the

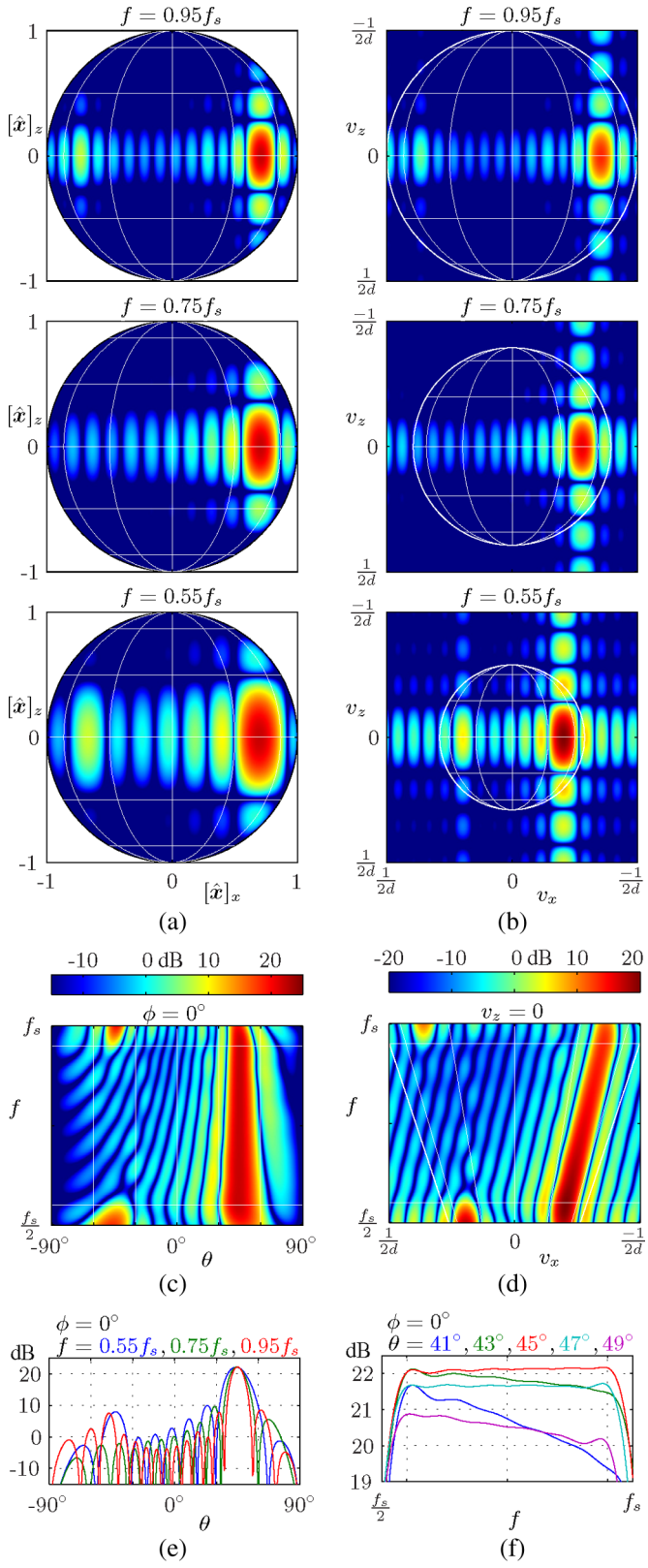

Fig. 6. Results of maximizing efficiency. (a) Array pattern directive gain. (b) Array factor. (c) Array pattern slice at $\phi = 0°$. (d) Array factor slice $v_z = 0$. (e) Angular response detail. (f) Frequency response detail.

array factor uniformly across the spatial-frequency period. The array-factor mainbeam width in spatial frequency is now nearly constant across temporal frequency. As a consequence, and in

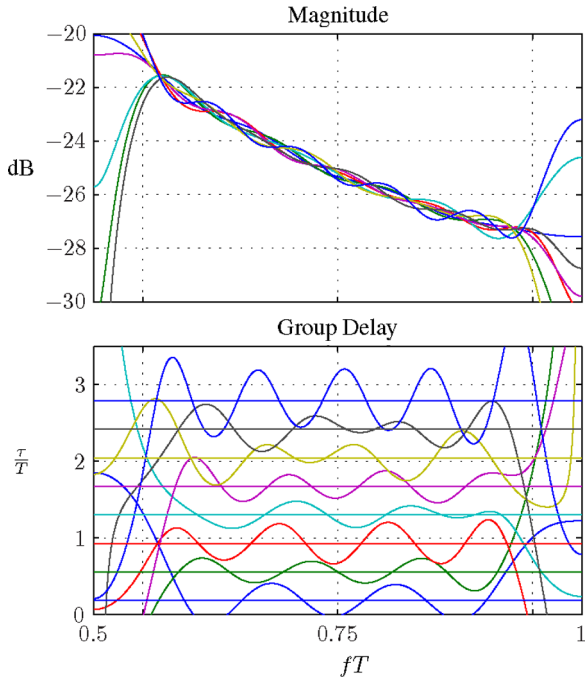

Fig. 7. Magnitude and group-delay responses of selected element filters for maximum-efficiency example design. Horizontal group-delay lines indicate theoretical ideal delay of the filter response of the corresponding color.

contrast to the previous example, the array-pattern mainbeam angular width here narrows with increasing frequency. The loss of directivity is evident at lower frequencies, where the mainbeam is much wider than in the previous example. A side-effect of the narrowing beam is that the frequency response at mainbeam angles offset from the steering direction exhibit noticeable rolloff at higher frequencies, as seen in Fig. 6(f).

2) Relating to the Time-Delay Solution: Let us now relax the requirement that the beamformer filters be FIR and set the passband error on the left in (23c) identically to zero by requiring that $\mathrm{B}(-\hat{\mathbf{x}}_0 f/c, f) = \mathrm{A}_0(f)/\mathrm{A}_{\mathrm{elV}}(-\hat{\mathbf{x}}_0 f/c, f)$. A straightforward application of the Cauchy-Schwarz inequality reveals that

$$|\mathrm{B}(\boldsymbol{v}, f)|^2 \leq K \sum_{\mathbf{x}\in\boldsymbol{\mathcal{L}}} |B(\mathbf{x}, f)|^2 \tag{24}$$

where K is the number of array elements. Subject to the above constraint, this bound is attained in the look direction (minimizing the integrand of (23b) pointwise, and thus also minimizing the integral) when

$$B(\mathbf{x}, f) = \frac{\mathrm{A}_0(f)}{K\mathrm{A}_{\mathrm{elV}}(-\hat{\mathbf{x}}_0 f/c, f)} e^{-\mathrm{j}2\pi \mathbf{x}\cdot\hat{\mathbf{x}}_0 f/c}. \tag{25}$$

This is just the classic time-delay solution for wideband pattern synthesis with a leading factor, common to all elements, that controls the desired array-pattern frequency response in the look direction. The drive current for each element is identical save a time delay by $\mathbf{x}\cdot\hat{\mathbf{x}}_0/c$ that depends on element position $\mathbf{x}$ and steering direction $\hat{\mathbf{x}}_0$. We thus expect that in the FIR solution the beamformer filters will approximate (25). This is verified in Fig. 7, which shows the magnitude and group-delay responses for the eight beamformer filters corresponding to elements located on the x-axis at positions $x = d/2, 3d/2, \ldots, 15d/2$. All filters have nearly the same magnitude response, as predicted.

(Excess gain in the transition bands is harmless, as the input is bandlimited.) On the group-delay plot, each horizontal line indicates the theoretical delay of one filter response. Although the group-delay curves have large error ripples, we can see that the mean group delay of each filter matches the theory. Given these relatively large group-delay and magnitude response ripples, it might seem surprising that the overall array-pattern passband could be made so flat. Indeed, had the filters been independently designed to approximate (25) then the passband specification might not have been met if the complex-error ripples in the individually designed filters added constructively in the array factor. Since we do not care about the individual approximation errors, the joint design is superior.

C. Wideband Gain and Power Gain

Although maximizing efficiency produced a reasonable design, it is clear from the definition that efficiency does not provide a measure of where the radiated power goes. Directivity provides a measure of how focused a beam is, but as we have seen optimizing wideband directivity alone leads to impractical designs. A metric which combines efficiency and wideband directivity is *wideband gain*, which we define over a frequency band $\mathcal{F}$ as the ratio of the average far-field power intensity in the direction $\hat{\mathbf{x}}_0$ to the average density that would result from a lossless isotropic radiator with the same input power

$$\mathcal{G}_0 \triangleq \frac{4\pi}{\mathcal{P}_{\text{in}}} \int_{\mathcal{F}} \mathcal{U}(\hat{\boldsymbol{x}}_0, f) df. \tag{26}$$

Comparing this to (15) and (22), we see that wideband gain is simply the product of efficiency and wideband directivity, $\mathcal{G}_0 = \xi \mathcal{D}_0$. Analogous to the relationship between wideband gain and wideband directivity, *wideband power gain* is defined as the product of efficiency and wideband directive gain $\mathcal{G}(\boldsymbol{x}, f) \triangleq \xi \mathcal{D}(\boldsymbol{x}, f)$. Power gain is often used in the place of directive gain to normalize array patterns.

Wideband gain measures how well the array converts input power into far-field radiation in a given direction. As such, it is usually a more appropriate metric than either wideband directivity or efficiency alone. If we again assume the input spectrum $|S(f)|^2 = T_s 1_{\mathcal{F}}(f) / \int_{\mathcal{F}} df$, then we can substitute (12) and (20) into (26) to derive a signal-independent definition of wideband gain as

$$\mathcal{G}_0 = \frac{\frac{1}{\eta} \int_{\mathcal{F}} \|\vec{\mathbf{A}}(-\hat{\boldsymbol{x}}_0 f/c, f)\|^2 df}{\frac{1}{4\pi} \int_{\mathcal{F}} \sum_{\mathbf{x},\mathbf{x}' \in \boldsymbol{\mathcal{L}}} B^*(\mathbf{x}, f) \text{Re}\{Z(\mathbf{x}, f; -\mathbf{x}')\} B(\mathbf{x}', f) df}. \tag{27}$$

If we additionally assume that $\mathcal{P}_{\text{loss}}$ is dominated by series element resistance, then we can use $\mathcal{P}_{\text{in}} = \mathcal{P}_{\text{rad}} + \mathcal{P}_{\text{loss}}$ and substitute (12), (13), and (21) into (26), to get (28), as shown at the bottom of the page. Top and bottom are both convex and quadratic in the beamformer coefficients. We can optimize wideband gain by fixing the numerator with a passband constraint as before, and minimize the denominator.

1) Example: Maximizing Wideband Gain: We can optimize the wideband gain of the example array by solving the SOC program

$$\min . \ \alpha > 0 \tag{29a}$$

$$\text{s.t.} \quad \frac{1}{\eta} \int_{\mathcal{F}} \int |\text{A}_{\text{V}}(-\hat{\boldsymbol{x}} f/c, f)|^2 \underline{\Omega}(d\boldsymbol{x}) df + Z_0 \int_{\mathcal{F}} \sum_{\mathbf{x} \in \boldsymbol{\mathcal{L}}} |B(\mathbf{x}, f)|^2 df \leq \alpha^2 \tag{29b}$$

$$\frac{1}{\int_{\mathcal{F}} df} \int_{\mathcal{F}} |\text{A}_{\text{V}}(-\hat{\mathbf{x}}_0 f/c, f) - \text{A}_0(f)|^2 df \leq 10^{-\frac{40}{10}}. \tag{29c}$$

The mainbeam passband constraint (29c) is the same as in the previous designs. Here it also serves to fix the numerator of (28), while the objective and SOC constraint (29b) combine to minimize the denominator (input power), thus maximizing wideband gain. This program was setup in 489 s and solved in 307 s. Maximum wideband gain was found to be 22.4 dB, with an efficiency of 90% and a wideband directivity of 22.9 dB. Fig. 8 shows the optimal array pattern and array factor. Compared to the previous example, the array-pattern mainbeam is somewhat narrower at lower frequencies, and has less variation in width over frequency. The array-pattern frequency response for off-center mainbeam directions still exhibits significant rolloff. The array factor now has larger invisible sidelobes, and there is a clear delineation between the visible sidelobes and the larger invisible sidelobes.

Comparing the three examples presented so far, it is clear that the maximum-directivity example is the outlier, with efficiency near zero and extremely small wideband gain. Of the other two designs, the maximum-gain design is clearly superior, as it has 0.7 dB more wideband directivity and 0.5 dB more wideband gain for very little loss in efficiency.

D. Other Constraints to Mitigate Superdirectivity

Previously we saw that constraining lost or input power serves to mitigate the undesired effects of optimizing directivity alone. We now consider two other constraint types that have a similar effect: sensitivity to channel-mismatch errors, and limits on individual driver outputs.

1) Sensitivity: It has long been known that superdirective narrowband arrays are extremely sensitive to uncompensated gain and position errors between the array channels [46], and the same is true of wideband arrays [11]. In this section, we present a basic wideband mean-square sensitivity analysis that considers only gain errors, but can be extended to include polarization errors and position errors also. Alternative approaches

$$\mathcal{G}_0 = \frac{\frac{1}{\eta} \int_{\mathcal{F}} \|\vec{\mathbf{A}}(-\hat{\boldsymbol{x}}_0 f/c, f)\|^2 df}{\frac{1}{4\pi\eta} \int_{\mathcal{F}} \int \|\vec{\mathbf{A}}(-\hat{\boldsymbol{x}} f/c, f)\|^2 \underline{\Omega}(d\boldsymbol{x}) df + \frac{Z_0}{4\pi} \int_{\mathcal{F}} \int |B(\boldsymbol{x}, f)|^2 \underline{\Sigma}_{\boldsymbol{\mathcal{L}}}(d\boldsymbol{x}) df}. \tag{28}$$

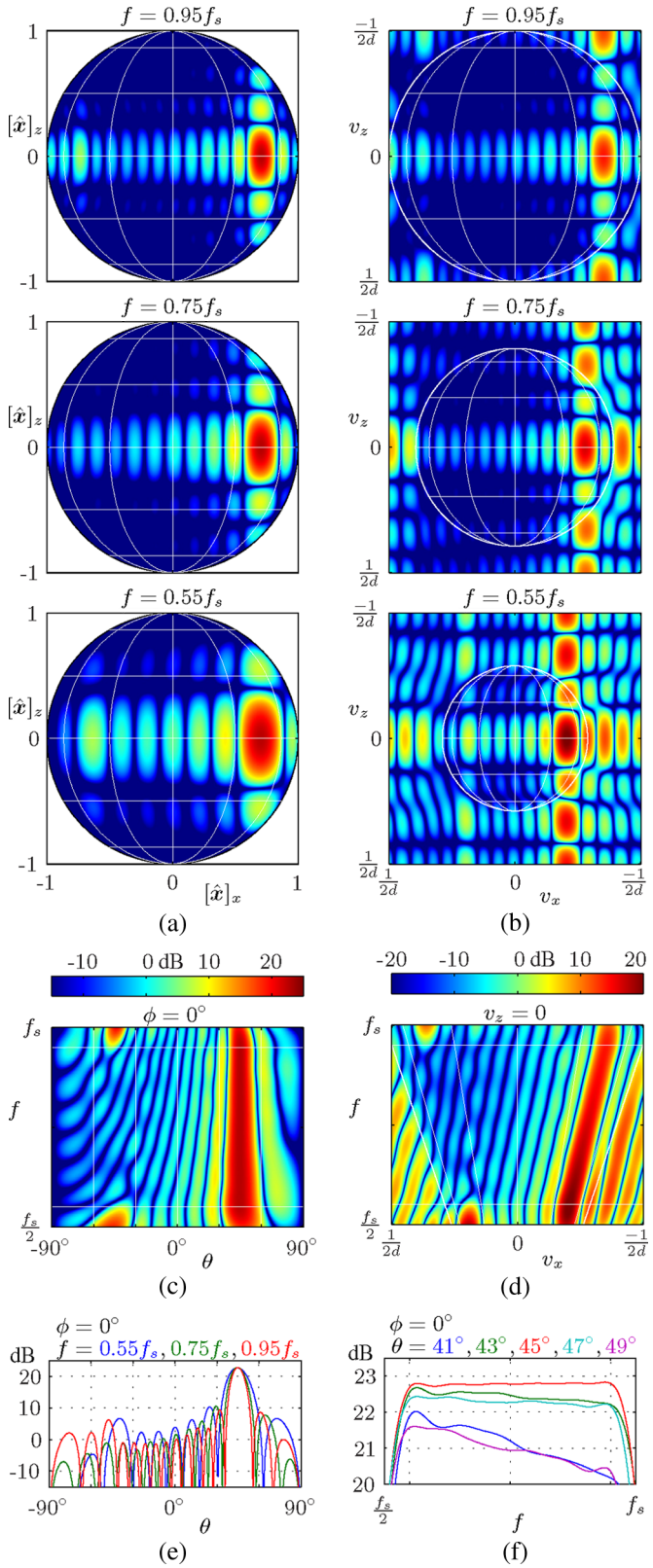

Fig. 8. Results of maximizing wideband gain. (a) Array pattern directive gain. (b) Array factor. (c) Array pattern slice at $\phi = 0°$. (d) Array factor slice at $v_z = 0$. (e) Angular response detail. (f) Frequency response detail.

exist [15] to instead bound the maximum error (so-called "robust optimization"), but since the number of constraints grows exponentially in K, these are impractical for large arrays.

We assume that, due to inevitable analog-hardware variations, the element patterns do not exactly match their ideal values. We will represent this as

$$\vec{\mathbf{A}}_{\mathrm{el}}(\boldsymbol{v}, f; -\boldsymbol{x}') = (1 + \zeta(\boldsymbol{x}'; \boldsymbol{v}, f))\, \vec{\mathbf{A}}_{\mathrm{el}_0}(\boldsymbol{v}, f; -\boldsymbol{x}')$$

where ζ is a random variable on element position $\boldsymbol{x}'$ parametrized on spatial and temporal frequency, and $\vec{\mathbf{A}}_{\mathrm{el}0}$ is the ideal element pattern. We will assume that these errors have zero mean and are uncorrelated from channel to channel, so that $r_\zeta(\boldsymbol{x}', \boldsymbol{y}'; \boldsymbol{v}, f) = \sigma_\zeta^2 1_{\{0\}}(\boldsymbol{y}' - \boldsymbol{x}')$. Now the antenna pattern is

$$\vec{\mathbf{A}}(\boldsymbol{v}, f) = \sum_{\boldsymbol{x}' \in \boldsymbol{\mathcal{L}}} \vec{\mathbf{A}}_{\mathrm{el}_0}(\boldsymbol{v}, f; -\boldsymbol{x}') \boldsymbol{B}(\boldsymbol{x}', f) + \sum_{\boldsymbol{x}' \in \boldsymbol{\mathcal{L}}} \zeta(\boldsymbol{x}'; \boldsymbol{v}, f) \vec{\mathbf{A}}_{\mathrm{el}_0}(\boldsymbol{v}, f; -\boldsymbol{x}') \boldsymbol{B}(\boldsymbol{x}', f)$$

the sum of the desired pattern $\vec{\mathbf{A}}_0(\boldsymbol{v}, f)$ and the *error pattern* $\vec{\mathbf{A}}_\zeta(\boldsymbol{v}, f)$. We now consider the expected value of the far-field power spectral intensity, which for a single input signal is proportional to the expected value of the power pattern $\|\vec{\mathbf{A}}\|^2$ by (12). Since the errors are uncorrelated, this is just the sum of the two component expected power patterns

$$E\left\{\left\|\vec{\mathbf{A}}(\boldsymbol{v}, f)\right\|^2\right\} = \left\|\vec{\mathbf{A}}_0(\boldsymbol{v}, f)\right\|^2 + \sigma_\zeta^2 \sum_{\boldsymbol{x}' \in \boldsymbol{\mathcal{L}}} \left\|\vec{\mathbf{A}}_{\mathrm{el}_0}(\boldsymbol{v}, f; -\boldsymbol{x}')\right\|^2 |B(\boldsymbol{x}', f)|^2 . \quad (30)$$

With all nominal element patterns identical, this reduces to

$$E\left\{\left\|\vec{\mathbf{A}}(\boldsymbol{v}, f)\right\|^2\right\} = \left\|\vec{\mathbf{A}}_{\mathrm{el}_0}(\boldsymbol{v}, f)\right\|^2 \times \left(|\mathrm{B}(\boldsymbol{v}, f)|^2 + \sigma_\zeta^2 \sum_{\boldsymbol{x}' \in \boldsymbol{\mathcal{L}}} |B(\boldsymbol{x}', f)|^2\right). \quad (31)$$

Now the common element pattern factors out, and we see that the remaining factor of the expected error pattern is not a function of spatial frequency (direction). At each frequency the error pattern sets a floor below which we expect array pattern features to be obscured, and (24) tells us that the error-pattern term in parenthesis in (31) is at least σ_ζ^2/K times the peak of the squared array factor. In most practical cases the peak-array-factor/error-pattern ratio will be within a few decibels of the bound, giving rise to common rules of thumb regarding the achievable sidelobe levels as a function of element count.

We can use SOCP to constrain, in mean square or pointwise across frequency, either the absolute error pattern or the error pattern relative to the desired pattern in the steering direction. Because we have limited or no spatial-frequency control over the error pattern and expect to be close to the Cauchy-Schwarz bound, these various approaches are likely to result in very similar designs. For the common-element case, perhaps the simplest approach would be to use a single SOC constraint to bound the mean-square value of the second (error) term inside the parenthesis of (31). Comparing to (23b), we see this is, to within a scale factor, exactly the expression we derived to constrain/minimize series power loss. Although not identical in general, constraints on power loss and constraints on sensitivity tend to "push" in the same direction, away from superdirectivity.

2) Element-Driver Constraints: Earlier we considered constraining the total input and lost power of the drivers. In many cases, we need to individually limit either the power or signal amplitude from each driver, for example to accommodate a fixed DAC output range. Constraining individual driver power is straightforward; the power from the driver at location $\boldsymbol{x}$ is obtained by unrolling the sum of (20)

$$\mathcal{P}_{\rm in}(\boldsymbol{x}) = \frac{1}{T_s}\int \sum_{\mathbf{x}'\in\boldsymbol{\mathcal{L}}} \boldsymbol{B}^*(\boldsymbol{x},f)\boldsymbol{S}^*(f) \times \mathrm{Re}\left\{Z(\boldsymbol{x},f;-\mathbf{x}')\right\}\boldsymbol{S}^T(f)\boldsymbol{B}^T(\mathbf{x}',f)df$$

which is convex and quadratic. Here we need K SOC constraints to limit peak driver power. More difficult is to constrain peak signal amplitude, as this depends on the temporal response of the input signals. If the maximum peak-to-rms ratio of the input signals is known, then we can instead constrain the mean-square value of each driver current. For a single input signal, this is

$$\frac{1}{T_s}\int |I(\boldsymbol{x},f)|^2\, df = \frac{1}{T_s}\int |S(f)|^2\, |B(\boldsymbol{x},f)|^2\, df \qquad (32)$$

and comparing to (21), we see this is proportional to the power lost to a series resistance in each channel. We previously showed that the ideal time-delay solution minimizes the total lost power, and as this solution evenly distributes the lost power across the channels it also minimizes (32) over $\boldsymbol{x}\in\boldsymbol{\mathcal{L}}$. (Actual FIR designs will differ slightly, or course.) This equivalence does not necessarily hold in the presence of other constraints, however, as the Cauchy-Schwarz bound of (24) is no longer attainable in general.

E. Mainbeam Frequency-Response Constraints

In the preceding examples, the mean-square frequency response error of a scalar array pattern was constrained only at the nominal beam steering direction $\hat{\mathbf{x}}_0$. This minimalist approach will be insufficient in two common cases: when polarization control is required, and when the target direction is not exactly known or is expected to be off-center. In the general case we will want to control the polarization as well as the complex amplitude of the response in order to match to a receive antenna. We can define desired and undesired scalar array pattern components $\mathrm{A}_{\|}$ and $\mathrm{A}_{\perp}$ by applying (10) to the array pattern with orthogonal Jones vectors $\vec{\boldsymbol{\psi}}_{\|}(f)$ and $\vec{\boldsymbol{\psi}}_{\perp}(f)$, respectively. We can then constrain the frequency-response error in $\mathrm{A}_{\|}$ in a mean-square, peak, or other sense while simultaneously constraining $\mathrm{A}_{\perp}$ to be "small". Although we design an array pattern to point in some nominal direction $\hat{\mathbf{x}}_0$, in practice the exact direction to a target is rarely known, and lies anywhere within some region around the beam center. As was shown in the previous examples, significant rolloff in the array-pattern frequency response occurs even for relatively small angular offsets from the beam center. It is tempting to consider adding many more constraints of the form (29c) over a dense grid of angles around $\hat{\mathbf{x}}_0$, but the result would be a flat-topped array pattern that would in turn result in reduced wideband gain. Instead, we would like to constrain the shape of the frequency response at a given angle without setting the overall level. Consider sets of passband constraint pairs of the form

$$\frac{1}{\int_{\mathcal{F}} df}\int_{\mathcal{F}} \left|\mathrm{A}_{\|}(-\hat{\mathbf{x}}_k f/c,f) - \beta_k \mathrm{A}_0(f)\right|^2 df \le \epsilon_{\|}^2\beta_k^2 \qquad (33a)$$

$$\frac{1}{\int_{\mathcal{F}} df}\int_{\mathcal{F}} \left|\mathrm{A}_{\perp}(-\hat{\mathbf{x}}_k f/c,f)\right|^2 df \le \epsilon_{\perp}^2,\ \ k=1,\ldots,K_{\rm mb} \qquad (33b)$$

where $\mathrm{A}_0(f)$ is the desired passband response, the set of locations $\{\hat{\mathbf{x}}_k\}$ discretizes the region of directions over which frequency-response control is desired, and $\epsilon_{\|}$ and $\epsilon_{\perp}$ are the root-mean-square desired-polarization and orthogonal-polarization errors, respectively. The $\{\beta_k\}$ are positive real auxiliary variables which are otherwise unconstrained and allowed to float, so that in direction $\hat{\mathbf{x}}_k$ the desired frequency response is $\beta_k\mathrm{A}_0(f)$. Fixing $\beta_0 = 1$ sets the scaling at the beam center, while the optimization process determines the rest of the β_k. In (33a), the mean-square error bound is made relative to the resulting frequency-response scaling by multiplying $\epsilon_{\|}$ by β_k^2 on the right. By contrast the orthogonal-polarization error in (33b) is shown bounded absolutely, but either can be constrained in either fashion as needed. This approach was used and illustrated in [21] for an array of orthogonal dipole pairs.

Alternatively we can bound the peak frequency response error of the desired and undesired components with constraint pairs of the form

$$\left|\mathrm{A}_{\|}(-\hat{\mathbf{x}}_k f_n/c,f_n) - \beta_k\mathrm{A}_0(f_n)\right| \le \gamma_{\|}\beta_k \qquad (34a)$$

$$\left|\mathrm{A}_{\perp}(-\hat{\mathbf{x}}_k f_n/c,f_n)\right| \le \gamma_{\perp},\quad k=1,\ldots,K_{\rm mb},\ n=1,\ldots,N_{\rm pb} \qquad (34b)$$

where $\mathrm{A}_0(f)$ and $\{\hat{\mathbf{x}}_k\}$ are as before, $\{f_n\}$ is a dense set of frequencies across the passband $\mathcal{F}$, and $\gamma_{\|}$ and $\gamma_{\perp}$ are the peak bounds on the frequency-response error in the desired and orthogonal components. Here the passband error is again defined relative to the nominal passband scaling β_k. If the array pattern is complex and the beamformer components do not have linear-phase symmetry, then each of (34a) and (34b) result in $K_{\rm mb}\times N_{\rm pb}$ rank-two SOC constraints. If either array pattern component has linear phase, then the corresponding line of (34) can be implemented as $K_{\rm mb}\times N_{\rm pb}$ pairs of linear constraints, which are more efficient to solve.

F. Sidelobe Constraints

Often it is necessary to explicitly constrain the sidelobe region, as simply optimizing gain or efficiency can result in relatively high close-in sidelobes. These metrics tend to have a stronger effect on the mainlobe than on the sidelobes because, to paraphrase bank robber Willie Sutton, that's where the power is. The mainlobe frequency-response constraints used in the previous section can also have the side effect of increasing sidelobes. Sidelobe constraints can be quite application-specific, for example providing extra suppression in the directions of ground clutter or known scatterers. In a shared array we might place extra constraints on the sidelobes of one pattern in the mainlobe direction of another pattern.

The suppression of sidelobes in array pattern design is analogous to stopband suppression in a frequency-selective filter, and

so many of the same approaches can be used. The most common metric is the peak array-pattern sidelobe level. Peak sidelobes can be constrained in the wideband sense by defining the sidelobe region in direction-frequency space, choosing a dense set of direction/frequency pairs $\{(\hat{\mathbf{x}}_k, f_k)\}$ across the region, and placing a constraint at each point. This results in the set of K_{sl} SOC constraints

$$\left\|\vec{\mathbf{A}}(-\hat{\mathbf{x}}_k f_k/c, f_k)\right\| \leq \gamma_{\mathrm{peak}}, \quad k = 1, \ldots, K_{\mathrm{sl}}$$

in general, and the set of $K_{\mathrm{sl}} \times N_{\mathrm{pb}}$ linear-constraint pairs

$$-\gamma_{\mathrm{peak}} \leq \left\|\vec{\mathbf{A}}_{\mathrm{el}}(-\hat{\mathbf{x}}_k f_k/c, f_k)\right\| \mathrm{B}(-\hat{\mathbf{x}}_k f_k/c, f_k) \leq \gamma_{\mathrm{peak}}$$

for $k = 1, \ldots, K_{\mathrm{sl}}$ when the element responses are all identical and the array factor is real. Here, γ_{peak} is the peak sidelobe height, which can be a constant or an optimization variable. Rather than constraining sidelobes pointwise across temporal frequency, we can choose a dense grid of directions $\{\hat{\mathbf{x}}_n\}$ across the sidelobe region and bound the mean-square (across frequency) sidelobes in each direction $\hat{\mathbf{x}}_k$ using N_{sl} SOC constraints of the form

$$\frac{1}{\int_{\mathcal{F}} df} \int_{\mathcal{F}} \left\|\vec{\mathbf{A}}(-\hat{\mathbf{x}}_n f/c, f)\right\|^2 df \leq \epsilon^2_{\mathrm{peak}}, \quad k = 1, \ldots, N_{\mathrm{sl}}$$

where ϵ_{peak} is the peak value of the mean-square sidelobes. Yet another approach is to constrain mean-square sidelobes across both temporal frequency and sidelobe direction, sometimes referred to as the *integrated sidelobe level* (ISL). This can be constrained with the single SOC

$$\frac{1}{\int_{\mathcal{F}} \int d\underline{\Omega}_{\mathrm{sl}}(\boldsymbol{x}) df} \int_{\mathcal{F}} \int \left\|\vec{\mathbf{A}}(-\hat{\boldsymbol{x}} f/c, f)\right\|^2 d\underline{\Omega}_{\mathrm{sl}}(\boldsymbol{x}) df \leq \epsilon^2_{\mathrm{rms}}$$

where surface-area measure $\underline{\Omega}_{\mathrm{sl}}$ defines the sidelobe region and ϵ_{rms} is the desired rms sidelobe level.

1) Example: Frequency-Response and Peak-Sidelobe Constraints: We augment the maximum-gain design example of (29) with the following mainbeam frequency-response and sidelobe constraints:

$$\frac{1}{\int_{\mathcal{F}} df} \int_{\mathcal{F}} \left|\mathrm{A_V}(-\hat{\mathbf{x}}_k f/c, f) - \beta_k \mathrm{A}_0(f)\right|^2 df \leq 10^{-\frac{40}{10}} \beta_k^2,$$
$$k = 1, \ldots, K_{\mathrm{mb}} \tag{35a}$$
$$\left|\mathrm{A_V}(-\hat{\mathbf{x}}_k f_k/c, f_k)\right| \leq 10^{-\frac{25}{20}}, \quad k = 1, \ldots, K_{\mathrm{sl}} \tag{35b}$$

In (35a) we have added $K_{\mathrm{mb}} = 24$ new main-beam frequency-response constraints in directions $\{\hat{\mathbf{x}}_k\}$, which range $\pm 4^\circ$ from $\hat{\mathbf{x}}_0$ in 2° steps in both azimuth and elevation. Each SOC constraint upper-bounds the relative mean-square error over $\mathcal{F}$ between the array pattern in direction $\hat{\mathbf{x}}_k$ and the product of real auxiliary variable β_k times desired response A_0 (here, unity). In (35b) we have added a -25 dB peak sidelobe constraint in the form of $K_{\mathrm{sl}} = 13591$ pairs of linear constraints spread evenly in spatial frequency across a sidelobe region defined in (ϕ, θ, f) space as $([-90^\circ, -25^\circ] \cup [25^\circ, 90^\circ]) \times ([-90^\circ, 30^\circ] \cup [66^\circ, 90^\circ]) \times \mathcal{F}$. Although asymmetric about the beam center in azimuth angle, it is symmetric in spatial frequency and thus leads to uniform transition bands in the array factor. Problem setup took 517 s while solving took 6510 s, the increase mainly due to the large number of peak constraints. The resulting responses are plotted

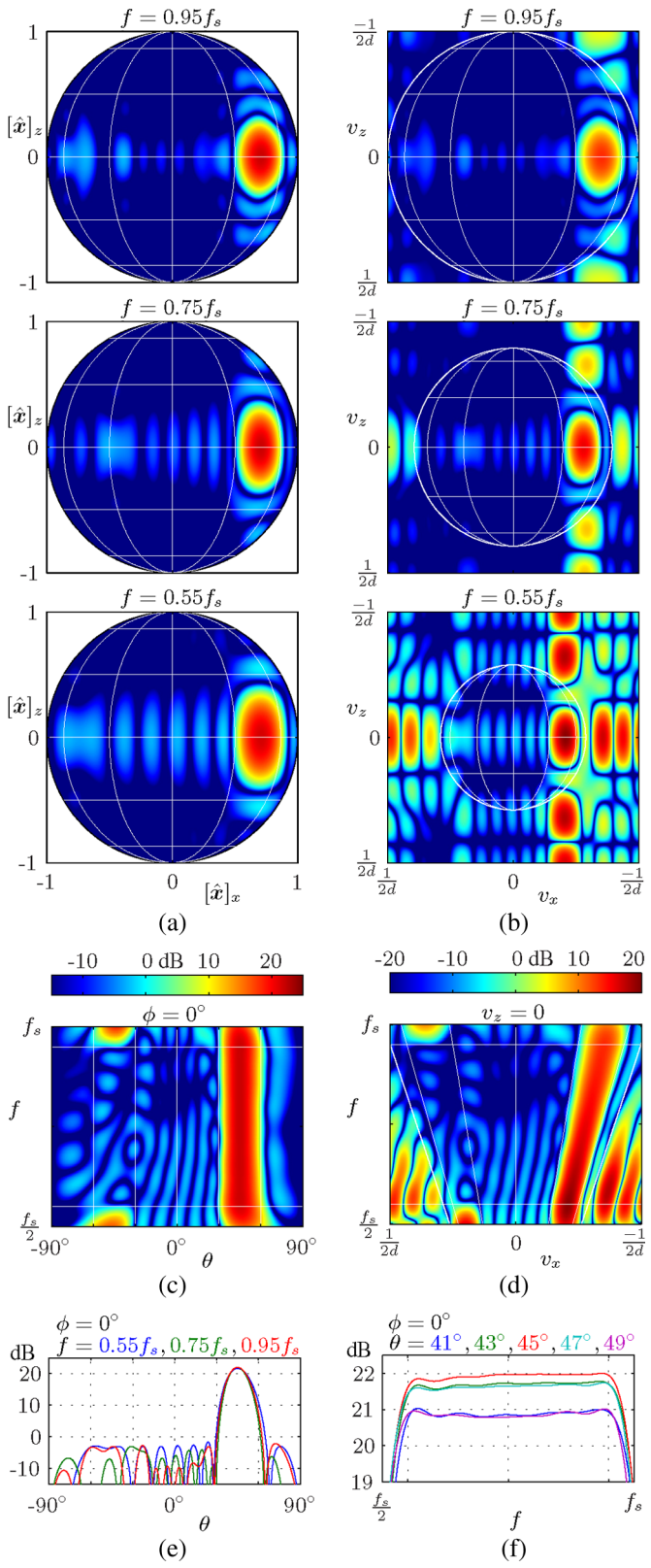

Fig. 9. Results of maximizing wideband gain subject to mean-square passband constraints in the mainlobe and peak constraints on the sidelobes. (a) Array pattern directive gain. (b) Array factor. (c) Array pattern slice at $\phi = 0^\circ$. (d) Array factor slice at $v_z = 0$. (e) Angular response detail. (f) Frequency response detail.

in Fig. 9. The direct effects of the added constraints can be seen in Fig. 9(f), showing that the frequency responses have indeed been flattened. In Fig. 9(c) and 9(e), we see that a side effect of the frequency-response constraints is to enforce an array pattern whose mainbeam has uniform width across frequency. Since it is not possible to efficiently narrow the mainbeam at lower frequencies, the result of the optimization is primarily to widen the mainbeam at higher frequencies. Mainbeam width in such designs is largely dictated by the lowest operating frequency. Meeting the peak-sidelobe constraints also caused an overall beam-broadening, an inevitable tradeoff. Wideband directivity, efficiency, and wideband gain are 22.0 dB, 89%, and 21.4 dB, respectively, the latter a loss of 0.7 dB from the previous example. The loss of wideband gain due to the additional constraints is largely reflected in a reduced wideband directivity, with efficiency essentially fixed.

V. Conclusion

In this paper, we have examined the problem of wideband array-pattern optimization for transmit arrays with linear amplification. By tracing signals in a simplified passband-equivalent model from input to the far field, we showed that the conventional analysis of narrowband arrays as spatial FIR filters extends from the usual 2-D narrowband case to more-interesting 3-D and 4-D space-time geometries. This aids in visualization, and the mapping from the visible array pattern to the Helmholtz cone in the spatio-temporal frequency domain explains, for example, why constraints only on radiated power result in underconstrained, superdirective solutions. Because the array pattern is linear in the beamformer coefficients and the constraints of interest are linear and convex quadratic, second-order cone programming is a natural choice. The large list of potential constraints presented speaks to the power and flexibility that SOCP provides for optimization of array patterns and other FIR-like structures. Through the series of examples, we have made connections to classic results (superdirectivity and time-delay steering), fitting them into the present framework and showing that we can improve both directivity and gain over the classic solutions while allowing a very general set of frequency-response and sidelobe constraints.

References

[1] J. O. Coleman, D. P. Scholnik, and J. J. Brandriss, "A specification language for the optimal design of exotic FIR filters with second-order cone programs," in *Proc. Asilomar Conf. Signals Systems and Computing*, Pacific Grove, CA, Nov. 2002.

[2] J. F. Sturm, "Using SeDuMi 1.02, a MATLAB toolbox for optimization over symmetric cones," *Optimiz. Methods and Software*, vol. 11–12, pp. 625–653, 1999, special issue on Interior Point Methods.

[3] K. Toh, M. Todd, and R. Tutuncu, "SDPT3—A Matlab software package for semidefinite programming," *Optimiz. Methods and Software*, vol. 11, pp. 545–581, 1999.

[4] R. Vanderbei, "LOQO: An interior point code for quadratic programming," *Optimiz. Methods and Software*, vol. 12, pp. 451–484, 1999.

[5] C. L. Dolph, "A current distribution for broadside arrays which optimizes the relationship between beam width and side-lobe level," *Proc. Inst. Radio Eng.*, vol. IRE-34, pp. 335–348, Jun. 1946.

[6] T. T. Taylor, "Design of line source antennas for narrow beamwidth and low sidelobes," *IRE Trans. Antennas Prop.*, vol. AP-3, p. 16, 1955.

[7] S. Haykin and J. Kessler, "Relation between the radiation pattern of an array and the two-dimensional disrete fourier transform," *IEEE Trans. Antennas Propagat.*, vol. AP-23, no. 3, pp. 419–420, May 1975.

[8] K. Nishikawa, T. Yamamoto, K. Oto, and T. Kanamori, "Wideband beamforming using fan filter," in *Proc. IEEE Int. Symp. Circuits and Systems*, San Diego, CA, May 1992, vol. 2, pp. 533–536.

[9] L. T. Bruton, "Three-dimensional cone filter banks," *IEEE Trans. Circuits Syst. I*, vol. 50, no. 2, pp. 208–216, Feb. 2003.

[10] H. Lebret and S. Boyd, "Antenna array pattern synthesis via convex optimization," *IEEE Trans. Signal Processing*, vol. 45, no. 3, pp. 526–532, Mar. 1997.

[11] D. P. Scholnik and J. O. Coleman, "Superdirectivity and SNR constraints in wideband array-pattern design," in *Proc. IEEE Int. Radar Conf.*, Atlanta, GA, May 2001.

[12] D. P. Scholnik and J. O. Coleman, "Formulating wideband array-pattern optimizations," in *Proc. IEEE Int. Symp. Phased Array Systems and Technology (ISPAST 2000)*, Dana Point, CA, May 2000.

[13] D. P. Scholnik and J. O. Coleman, "Optimal design of wideband array patterns," in *Proc. IEEE Int. Radar Conf. (RADAR 2000)*, Alexandria, VA, May 2000.

[14] S. Yan and Y. Ma, "Design of FIR beamformer with frequency invariant patterns via jointly optimizing spatial and frequency responses," in *Proc. Int. Conf. Acoustics, Speech, and Signal Processing*, Mar. 2005, vol. 4.

[15] F. Wang, V. Balakrishnan, P. Y. Zhou, J. J. N. Chen, R. Yang, and C. F. C. , "Optimal array pattern synthesis using semidefinite programming," *IEEE Trans. Signal Process.*, vol. 51, no. 5, pp. 1172–1183, May 2003.

[16] C.-Y. Tseng and L. J. Griffiths, "A simple algorithm to achieve desired patterns for arbitrary arrays," *IEEE Trans. Signal Process.*, vol. 40, no. 11, pp. 2737–2746, Nov. 1992.

[17] L. I. Vaskelainen, "Iterative least-squares synthesis methods for conformal array antennas with optimized polarization and frequency properties," *IEEE Trans. Antennas Propagat.*, vol. 45, no. 7, pp. 1179–1185, Jul. 1997.

[18] M. Dinnichert, "Full polarimetric pattern synthesis for an active conformal array," in *Proc. IEEE Int. Symp. on Phased Array Systems and Technology*, Dana Point, CA, May 2000.

[19] G. Cardone, G. Cincotti, and M. Pappalardo, "Design of wide-band arrays for low side-lobe level beam patterns by simulated annealing," *IEEE Trans. Ultrason., Ferroelect., Freq. Contr.*, vol. 49, no. 8, pp. 1050–1059, Aug. 2002.

[20] D. B. Ward, R. A. Kennedy, and R. C. Williamson, "Theory and design of broadband sensor arrays with frequency invariant far-field beam patterns," *J. Acoust. Soc. Amer.*, vol. 97, no. 2, pp. 1023–1034, Feb. 1995.

[21] J. O. Coleman, D. P. Scholnik, and P. E. Cahill, "Synthesis of a polarization-controlled pattern for a wideband array by solving a second-order cone program," in *Proc. 2005 IEEE AP-S Int. Symp.*, Washington, DC, Jul. 2005.

[22] D. P. Scholnik, "Shared Wideband Transmit Antenna Arrays: Optimal Pattern Synthesis and Spatio-Temporal Delta-Sigma Modulation," Ph.D. dissertation, University of Maryland, Baltimore, MD, Jan. 2006.

[23] D. P. Scholnik, J. O. Coleman, D. Bowling, and M. Neel, "Spatio-temporal delta-sigma modulation for shared wideband transmit arrays," in *Proc. IEEE Radar Conf.*, Philadelphia, PA, Apr. 2004.

[24] J. O. Coleman, "A measure-convolution approach to elementary signals and systems," in *Proc. Conf. on Information Sciences and Systems*, Baltimore, MD, Mar. 1999.

[25] M. J. Lighthill, *Introduction to Fourier Analysis and Generalized Functions*. Cambridge, U.K.: Cambridge University Press, 1978.

[26] D. W. Kammler, *A First Course in Fourier Analysis*. Upper Saddle River, NJ: Prentice-Hall, 2000.

[27] H. L. Royden, *Real Analysis*. Upper Saddle River, NJ: Prentice-Hall, 1988.

[28] W. Rudin, *Fourier Analysis on Groups*. New York: Interscience, 1962.

[29] C. A. Balanis, *Antenna Theory*. : John Wiley & Sons, Inc., 1982.

[30] L. C. Shen and J. Kong, *Applied Electromagnetism*. Boston, MA: PWS Publishers, 1987.

[31] S. Akkarakaran and P. P. Vaidyanathan, "Bifrequency and bispectrum maps: A new look at multirate systems with stochastic inputs," *IEEE Trans. Signal Process.*, vol. 48, no. 3, pp. 723–736, Mar. 2000.

[32] R. C. Jones, "New calculus for the treatment of optical systems," *J. Opt. Soc. Amer.*, vol. 31, pp. 488–493, 1941.

[33] M. S. Lobo, L. Vandenberghe, S. Boyd, and H. Lebret, "Applications of second-order cone programming," *Linear Algebra and Its Applic.*, vol. 284, pp. 193–228, Nov. 1998.

[34] J. O. Coleman, "Systematic mapping of quadratic constraints on embedded FIR filters to linear matrix inequalities," in *Proc. 1998 Conf. Information Sciences and Systems (CISS '98)*, Princeton, NJ, Mar. 1998.

[35] J. O. Coleman and D. P. Scholnik, "Design of nonlinear-phase FIR filters with second-order cone programming," in *Proc. 1999 Midwest Symp. Circuits and Systems (MWSCAS '99)*, Las Cruces, NM, Aug. 1999.

[36] S. A. Schelkunoff, "A mathematical theory of arrays," *Bell Sys. Tech. J.*, vol. 22, pp. 80–107, Jan. 1943.
[37] C. J. Bouwkamp and N. G. deBruijn, "The problem of optimum antenna current distribution," *Philips Res. Rep.*, vol. 1, pp. 135–158, 1946.
[38] H. J. Riblet, "Note on the maximum directivity of an antenna," *Proc. I.R.E.*, vol. 36, pp. 620–624, May 1948.
[39] A. Bloch, R. G. Medhurst, and S. D. Pool, "Note on the maximum directivity of an antenna," *Proc. Inst. Radio Eng.*, vol. 48, no. 6, p. 1164, Jun. 1960.
[40] Y. T. Lo, S. W. Lee, and Q. H. Lee, "Optimization of directivity and signal-to-noise ratio of an arbitrary antenna array," *Proc. IEEE*, vol. 54, no. 8, pp. 1033–1045, Aug. 1966.
[41] M. M. Dawoud and A. Anderson, "Design of superdirective arrays with high radiation efficiencies," *IEEE Trans. Antennas Propag.*, vol. 26, pp. 819–823, 1978.
[42] E. H. Newman, J. H. Richmond, and C. H. Walter, "Superdirective receiving arrays," *IEEE Trans. Antennas Propag.*, vol. AP-26, no. 5, pp. 629–635, Sep. 1978.
[43] R. C. Hansen, "Superconductive antennas," *IEEE Trans. Aerosp. Electron. Syst.*, vol. 26, no. 2, pp. 345–355, Mar. 1990.
[44] H. Bohr, *Almost Periodic Functions*. New York: Chelsea, 1947.
[45] B. M. Levitan and V. V. Zhikov, *Almost Periodic Functions and Differential Equations*. Cambridge, U.K.: Cambridge Univ. Press, 1982.
[46] E. N. Gilbert and S. P. Morgan, "Optimum design of directive antenna arrays subject to random variation," *Bell Syst. Tech. J.*, vol. 34, pp. 637–663, May 1955.

Dan P. Scholnik (S'97–M'04) received the B.S. and M.S. degrees from Michigan Technological University, Houghton, in 1995 and 1997 and the Ph.D. degree from the University of Maryland, Baltimore County, in 2006, all in electrical engineering.

Since 1995, he has been with the Radar Division of the Naval Research Laboratory, Washington, DC. His research interests include optimal filter and array-pattern design, temporal and spatio-temporal delta-sigma D/A conversion, and synthetic-wideband radar waveform design.

Jeffrey O. Coleman (S'75-M'79-SM'99) received the B.S.E.E. degree from Massachusetts Institute of Technology, Cambridge, in 1975, the M.S.E.E. degree from Johns Hopkins University, Baltimore, MD, in 1979, and the Ph.D. degree from the University of Washington in 1991.

He was with the Radar Division of the Naval Research Laboratory (NRL), Washington, DC, from 1978 to 1985, then spent time in graduate studies and with The Boeing Company and Michigan Technological University, Houghton. He returned to NRL in 1997, where his research is on theory and design methods in digital signal processing.